Metabolite interactions in the bacterial Calvin cycle and implications for flux regulation

Emil Sporre[1]*, Jan Karlsen[1]*, Karen Schriever[2], Johannes Asplund Samuelsson[1], Markus Janasch[1], David Kotol[1], Linnéa Strandberg[1], Luise Zeckey[1], Ilaria Piazza[3], Per-Olof Syrén[2], Fredrik Edfors[1], Elton P. Hudson[1a].

[1] Department of Protein Science, Science for Life Laboratory, KTH - Royal Institute of Technology, Stockholm, Sweden
[2] Department of Fiber and Polymer Technology, Science for Life Laboratory, KTH - Royal Institute of Technology, Stockholm, Sweden
[3] Max Delbrück Center for Molecular Medicine in the Helmholtz Association (MDC Berlin), Berlin, Germany
* equal contribution
[a] correspondence: paul.hudson@scilifelab.se

Abstract

Metabolite-level regulation of enzyme activity is important for coping with environmental shifts in bacteria. Improved understanding of such regulation could guide attempts to engineer more efficient strains for biochemical production. Recently developed proteomics methods allow for mapping of post-translational interactions, including metabolite-protein interactions, that may be relevant for quickly regulating pathway activity. While feed-back and feed-forward regulation in glycolysis has been investigated, there is relatively little study of metabolite-level regulation in the Calvin cycle, particularly in bacteria. Here, we applied limited proteolysis small molecule mapping (LiP-SMap) to identify and compare metabolite-protein interactions in four potential metabolic engineering host that fix CO_2 using the Calvin cycle, including two photoautotrophs (cyanobacteria) and two chemoautotrophs. Species-specific interactions were observed, such as interactions with glucose-6-phosphate in the chemoautotroph *Cupriavidus necator* and interactions with glyoxylate in the cyanobacteria *Synechocystis sp.* PCC 6803, which suggests that metabolite-level regulation could be adapted to a certain metabolic capacity or lifestyle of these bacteria. Identified metabolite interactions with Calvin cycle enzymes fructose-1,6/sedoheptulose-1,7-bisphosphatase (F/SBPase) and transketolase were tested for effects on catalytic activity using kinetic assays. GAP increased the activity of both *Synechocystis* and *Cupriavidus* F/SBPase, which may act as a feed-forward activation mechanism in the Calvin cycle. A kinetic model incorporating regulations on F/SBPase generally enhanced flux control of ATP and NADPH supply over the cycle. We show that LiP-SMap is a promising technique to explore and uncover novel post-translational metabolic regulation, although the method could benefit from improved sensitivity and specificity.

Abbreviations

2OG 2-oxoglutarate
2PG 2-phosphoglycolate
3PGA 3-phosphoglycerate
6PG 6-phosphogluconate
AcCoA Acetyl-CoA
ADP Adenosine diphosphate
AGPase ADP-glucose synthase (EC 2.7.7.27)
AMP Adenosine monophosphate
ATP Adenosine triphosphate
cAMP Cyclic adenosine monophosphate
Cit Citrate
DAHPS 3-Deoxy-D-arabinoheptulosonate 7-phosphate synthase (EC 2.5.1.54)
dPGM 2,3-diphosphoglycerate-dependent phosphoglycerate mutase (EC 5.4.2.11)
ENO Enolase (EC 4.2.1.11)
FBA Fructose-bisphosphate aldolase (EC 4.1.2.13)
FBP Fructose-1,6-bisphosphate
FBPase Fructose-1,6-bisphosphatase (EC 3.1.3.11)
F/SBPase Bifunctional fructose-1,6/sedoheptulose-1,7-bisphosphatase (EC 3.1.3.11)
G6P Glucose-6-phosphate
G6PDH Glucose-6-phosphate dehydrogenase (EC 1.1.1.49)
GAP Glyceraldehyde-3-phosphate
GAPDH Glyceraldehyde-3-phosphate dehydrogenase (EC 1.2.1.12, 1.2.1.13, 1.2.1.59)
Glyc Glycolate
Glyx Glyoxylate
GPM Phosphoglucomutase (EC 5.4.2.2)
GTP Guanosine triphosphate
iPGM 2,3-diphosphoglycerate-independent phosphoglycerate mutase (EC 5.4.2.12)
KDPG 2-dehydro-3-deoxy-D-gluconate-6-phosphate
Mal Malate
NADP Nicotinamide adenine dinucleotide phosphate (oxidized)
NADPH Nicotinamide adenine dinucleotide phosphate (reduced)
PEP Phosphoenolpyruvate
PGI Phosphoglucoisomerase (EC 5.3.1.9)
PGK Phosphoglycerate kinase (EC 2.7.2.3)
Phe Phenylalanine
PRK Phosphoribulokinase (EC 2.7.1.19)
PYK Pyruvate kinase (EC 2.7.1.40)
RPE Ribulose-phosphate 3-epimerase (EC 5.1.3.1)
RPI Ribose-5-phosphate isomerase (EC 5.3.1.6)
RPPK Ribose-5-phosphate pyrophosphokinase (EC 2.7.6.1)
Ru5P Ribulose–5-phosphate
Rubisco Ribulose-bisphosphate carboxylase (EC 4.1.1.39)
RuBP Ribulose-1,5-bisphosphate
SBPase Sedoheptulose-1,7-bisphosphatase (EC 3.1.3.37)
SerA Phosphoglycerate dehydrogenase (EC 1.1.1.95)
Suc Sucrose
TAL Transaldolase (EC 2.2.1.2)
TKT Transketolase (EC 2.2.1.1)
TPI Triose-phosphate isomerase (EC 5.3.1.1)

Introduction

Metabolite-protein interactions are increasingly appreciated as feedback mechanisms for adapting metabolic flux to changing conditions (Link et al., 2013; Zampieri et al., 2019), as well as targets for metabolic engineering (Foster et al., 2022). Inference of allosteric regulation in metabolic networks has been done through analysis of time-resolved metabolite and proteomics datasets (Lempp et al., 2019; Link et al., 2013), fitting of multi-omics steady state data (Hackett et al., 2016; Nishiguchi et al., 2020), as well as with interaction proteomics techniques such as coelution of proteins and metabolites from a chromatography column (Veyel et al. 2018; Li et al. 2010; Guerreiro et al. 2016), and changes in protein stability during environmental perturbation (Savitski et al. 2014; Tan et al. 2018; Mateus et al. 2018; Pattanayak et al. 2020).

Limited proteolysis-coupled mass spectrometry (LiP-MS) detects changes in protease digestion patterns of a protein that occurs when it undergoes conformational change or binds to other proteins or effectors, without reliance on immuno-based enrichment or crosslinking (Mateus et al., 2021). LiP-MS performed on the proteome of yeast grown on ethanol showed that hundreds of proteins had different digestion patterns when compared to sugar-grown cells, indicating post-translational regulation during substrate shifts (Feng et al., 2014b). A variant of LiP-MS performs proteinase K digestion of the extracted proteome in the presence of an added metabolite (LiP-SMap; limited proteolysis-small molecule mapping). In LiP-SMap, interactions between proteins and metabolites are revealed by comparison of digestion patterns with or without the added metabolite (Piazza et al., 2018).
To demonstrate and benchmark the LiP-SMap technique, Piazza et al. treated yeast and *E. coli* extracts with metabolites and monitored changes in the LiP digestion patterns (Piazza et al., 2018). Hundreds of novel metabolite-protein interactions were detected, and in many cases the altered peptides could be mapped near the enzyme active site.

A relatively unexplored application area for interaction proteomics is the Calvin cycle, present in diverse bacteria as well as eukaryotic algae and plants. The bacterial Calvin cycle is of biotechnological interest as cyanobacteria and chemoautotrophic bacteria have been modified to produce biochemicals from carbon dioxide using sunlight, electricity, or hydrogen as energy sources (Koch et al., 2020; Krieg et al., 2018; Liu et al., 2019; Müller et al., 2013). An understanding of metabolite-level regulation of Calvin cycle enzymes, or metabolic pathways where the Calvin cycle is enmeshed, could inform metabolic engineering strategies. The Calvin cycle is susceptible to instability at branch points where intermediates are drained, and the kinetic parameters of cycle enzymes and branching enzymes are constrained (Barenholz et al., 2017; Janasch et al., 2019). Modulation of enzyme kinetic parameters (K_M, K_i, k_{cat}, Hill coefficient) such as by allosteric or competitive effectors, could affect cycle stability. While regulation of the Calvin cycle enzymes in plants has been extensively studied (Martin et al., 2000; Michelet et al., 2013; Raines, 2003), the Calvin cycle in bacteria is less characterized, particularly with respect to potential post-translational regulation. In light of the widespread distribution of the bacterial Calvin cycle, regulation may be different across species.

The freshwater cyanobacterium *Synechocystis sp.* PCC 6803 (*Synechocystis*) is a facultative heterotroph and is a model for studying photosynthesis. *Synechococcus elongatus* PCC 7942 (*Synechococcus*) is an obligate photoautotroph, and a model strain for

studying the circadian rhythm. It was found that *Synechocystis* contains a larger number of isoenzymes than *Synechococcus,* which may be related to its metabolic versatility (Beck et al., 2012; Jablonsky et al., 2016). The extent of post-translational regulation in the Calvin cycle in cyanobacteria is not clear. Quantitative proteomics and fluxomics of *Synechocystis* showed abundances of many Calvin cycle enzymes changed only weakly over a range of growth rates (Jahn et al., 2018; Yu King Hing et al., 2021; Zavřel et al., 2019). Insertion of heterologous sucrose synthesis in *Synechococcus* increased CO_2 uptake up to 30%, with only Rubisco and carboxysomes showing increased protein abundances (Singh et al., 2022). In contrast, insertion of ethanol biosynthesis in *Synechocystis*, which stimulated carbon fixation significantly, did lead to increased abundance of multiple Calvin cycle enzymes (Borirak et al., 2015). Comparisons of the transcriptomic response to changes in inorganic carbon supply suggest that *Synechocystis* responds primarily through biochemical regulation of enzyme fluxes, while *Synechococcus* responds at the transcriptional level (Jablonsky et al., 2016; Klähn et al., 2015; Schwarz et al., 2011). Thus, central carbon metabolism in these two species may be regulated differently, with respect to potential metabolite inhibition or activation of enzymes.

The Calvin cycle is present in roughly 7 % of non-cyanobacterial genomes (Asplund-Samuelsson and Hudson, 2021). Microbes harboring the Calvin cycle may have a growth advantage in environments poor in organic substrates, due to improved cofactor recycling, or in environments with mixed or fluctuating carbon sources (McKinlay and Harwood 2010; Jahn et al. 2021). Nevertheless, knowledge of Calvin cycle regulation in chemoautotrophs is limited. *Cupriavidus necator* (*Cupriavidus*) and *Hydrogenophaga pseudoflava* (*Hydrogenophaga*) are chemoautotrophic betaproteobacteria in the order Burkholderiales. *Cupriavidus* acquired the Calvin cycle on a megaplasmid, where genes encoding all cycle enzymes are clustered as an operon. The *ccb* operon is duplicated on the chromosome (Kusian and Bowien, 1997; Pohlmann et al., 2006). The Calvin cycle of *Hydrogenophaga* is similarly clustered on the chromosome (Grenz et al., 2019; Meyer and Schlegel, 1978). To date, most study on regulation of Calvin cycle activity in chemoautotrophs has focused on transcriptional regulation, where the transcriptional activator of the Calvin cycle operator CbbR has multiple metabolite effectors that may depended on species (Bowien and Kusian, 2002; Dangel and Tabita, 2015).

Here, we applied the LiP-SMap technique to uncover new regulatory metabolite interactions with central carbon metabolism enzymes in four bacterial strains containing the Calvin cycle, *Synechocystis sp.* PCC 6803, *Synechococcus* PCC 7942, *Cupriavidus necator* (formerly *Ralstonia eutropha*), and *Hydrogenophaga pseudoflava.* Species-specific interaction patterns for several metabolites such as GAP, G6P and glyoxylate were found, which indicates that enzyme regulation by these metabolites could differ between autotrophic organisms. Complementary *in vitro* assays showed that GAP increases the catalytic activity of both *Synechocystis* and *Cupriavidus necator* F/SBPase, suggesting a feed-forward activation mechanism in the Calvin cycle.

Results

Assessment of LiP-SMap method and data

The LiP-SMap protocol developed by Piazza et al. was applied in the current study with minor modifications (Piazza et al., 2018). Extracted proteomes were first filtered to remove endogenous metabolites and resuspended in a buffer containing 1 mM $MgCl_2$. Metabolite was added to four aliquots of the proteome extract, while buffer was added to another four aliquots as negative controls. Extracts were then digested partially by proteinase K (LiP), followed by tryptic digestion with a mixture of trypsin and LysC to enable peptide quantification using liquid chromatography-mass spectrometry. Any peptide that was differentially abundant ($q < 0.01$) in the metabolite-treated condition versus the control condition was assigned as a metabolite interaction. Proteins with at least one metabolite-interacting peptide were assigned as a metabolite-interacting protein (**Figure 1**, Material and Methods).

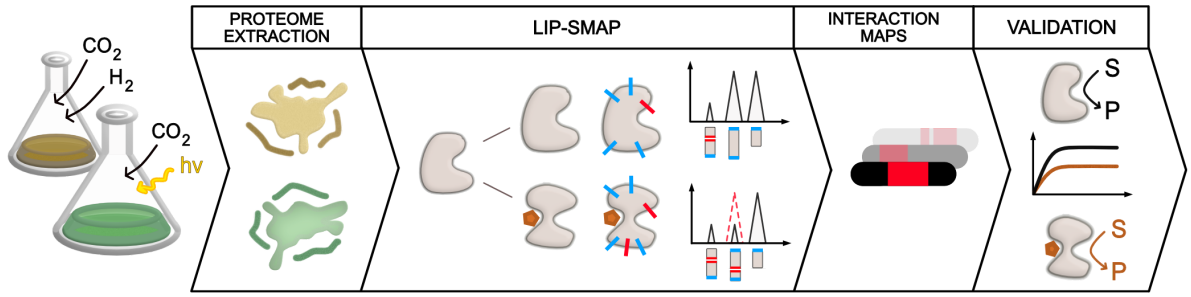

Figure 1. Workflow for interaction proteomics and validation on cyanobacteria and lithoautotrophic bacteria. LiP-SMap: Limited proteolysis small molecule mapping (Piazza et al., 2018).

To demonstrate the capability of LiP-SMap to detect changes in protein structure, we first tested the effect of reducing and oxidizing agents (Dithiothreitol (DTT) and 5,5′-dithiobis-2-nitrobenzoic acid (DTNB), respectively) on the extracted proteome of *Synechocystis.* Addition of DTT to 1 mM, a concentration chosen to induce specific redox effects in extracts (Alliegro, 2000), resulted in altered peptides in 21 proteins, a small number that indicates that *Synechocystis* proteome extracts are likely in a reduced state. By contrast, addition of DTNB to 50 µM, a concentration shown to completely inhibit cyanobacteria phosphoribulokinase (PRK) *in vitro* (Kobayashi et al., 2003), altered peptides from 129 proteins, including PRK and Rubisco (**Figure S1, Dataset S1**). These results indicate that LiP-SMap can detect the changes in protein structure mediated by reducing and oxidizing agents.

The sensitivity of detecting metabolite-interacting proteins with LiP-SMap depends on the number of detected peptides within each protein; a low peptide coverage will reduce the number of detected interactions. A total of 8,000-15,000 peptides were detected in each LiP-SMap experiment (**Figure S2, Dataset S2**), and a higher number of peptides were detected in metabolite-interacting proteins than in non-interacting proteins (**Figure S3**). The

peptide coverage of Calvin cycle enzymes was generally high, averaging 17 peptides per enzyme (minimum 5, maximum 40), with sequence coverage approximately 50% (**Figure 2**). To gauge the technical reproducibility of the LiP-SMap method, we compared the results from two consecutive LiP-SMap procedures prepared from the same *Cupriavidus* cell sample, testing three metabolite treatments: AcCoA (1 and 10 mM) and ATP (32 mM). The agreement in detected metabolite-interacting proteins between replicates ($q < 0.01$) was higher than expected by random chance, but 36-74% of the interactions were detected in only one replicate (**Figure S4**). The lower reproducibility of AcCoA interactions are presumably related to a poor trypsin digestion detected in the first LiP-SMap run. Proteins with a high peptide coverage are more likely to be falsely assigned as a metabolite-interacting protein, since one single falsely assigned peptide change is sufficient to assign the whole protein as interacting. This was reflected in a larger fraction of non-reproducible metabolite-interacting proteins among proteins with the highest number of detected peptides (top 25%).

Metabolites were tested at one high and one low concentration (**Tables S1 and S2**). There were more detected interactions from the high concentrations than at the low concentrations. Typically > 80% of interactions from low-concentration treatment were also observed in the high-concentration treatment, adding confidence to interactions observed from both (**Figure S5**). We did not observe strong dose effects between the two concentrations, though ATP and GTP interactions were exceptions (**Figure S6**). A significantly altered peptide degradation rate during LiP induced by a higher metabolite concentration will have a limited impact on the quantified peptide abundance after LiP if the amount of degraded peptide is low compared to the total amount of the peptide (protein) in the proteome extract. For example, if the degradation of a certain peptide increases threefold from 10 to 30%, the quantified peptide abundance will only decrease 1.3-fold, from 90 to 70%. In some cases, insensitivity to concentration could indicate that metabolite-protein binding events are already saturated at the low concentration (typically 1 mM).

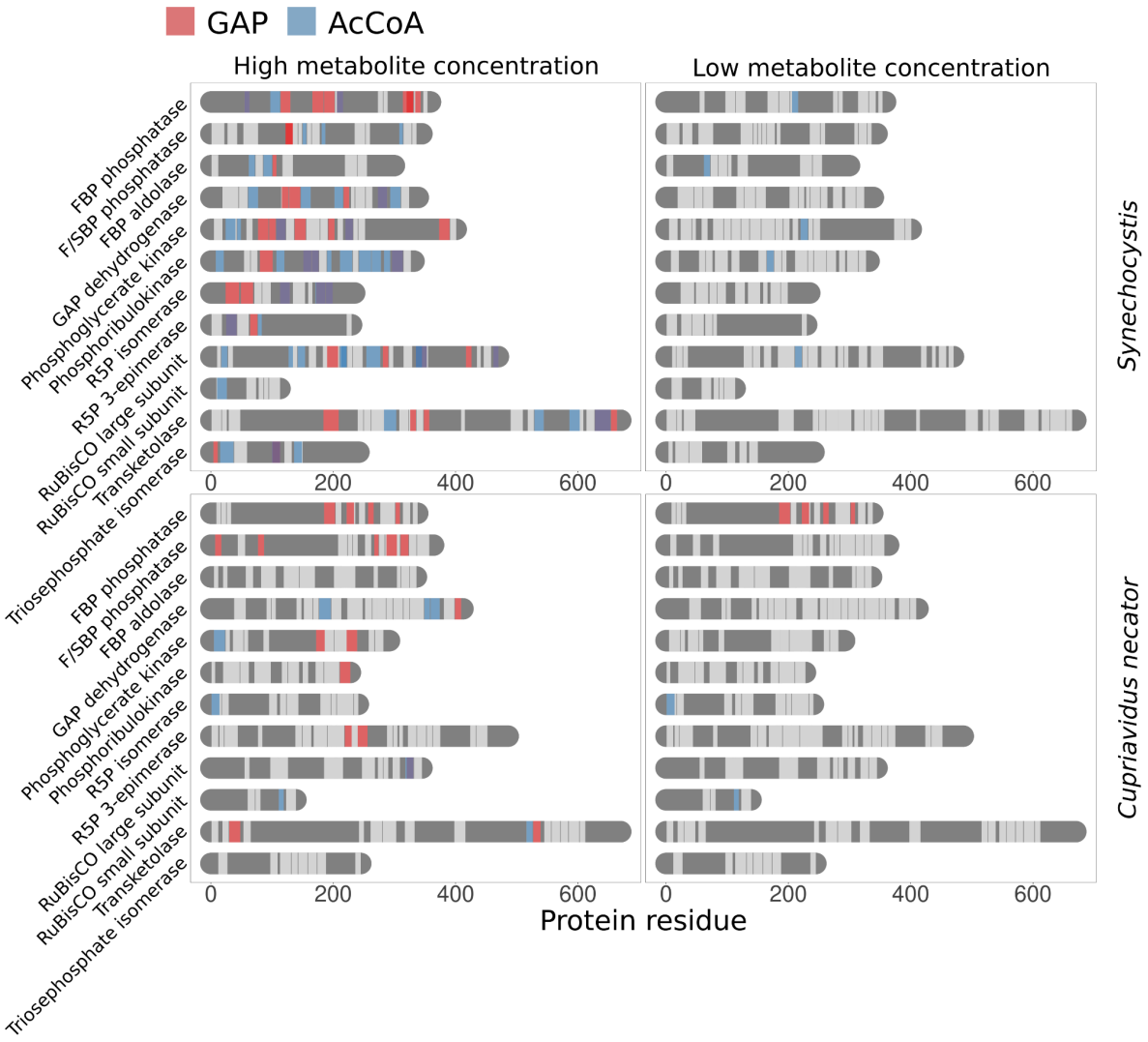

Figure 2. Peptide coverage of Calvin cycle enzymes was on average 50%. The figure displays a representation (GAP and AcCoA) of LiP-SMap-detected peptides within Calvin cycle enzymes of *Synechocystis* and *Cupriavidus*. Peptides showing a significant change in abundance in response to added metabolite are highlighted in color, while other detected peptides are light gray. Peptides depicted in purple were significantly changed in response to both GAP and AcCoA treatment. For high concentration tests, 5 mM GAP or 10 mM AcCoA was added. For low concentration tests, 0.5 mM GAP or 1 mM AcCoA was added.

Interactions of selected metabolites with Calvin cycle and surrounding enzymes

All four bacteria use the Calvin cycle to fix CO_2 but differ in terms of phylogeny, energy source, substrate utilization, and natural habitats. Conserved metabolite-induced regulation in these microbes may therefore be important for autotrophic metabolism in general, while differences may indicate adaptations specific to a certain microbial lifestyle or evolutionary trajectory. To identify such regulatory features, up to 25 metabolites were screened for interactions with proteome extracts of *Synechocystis* (25), *Synechococcus* (21),

Cupriavidus (23)*, and Hydrogenophaga* (8). Metabolites were chosen based on their potential to act as a regulatory signal or as a signal of energy, redox or metabolic status of the cell (e.g. metabolites located in metabolic pathway branch/end points). Two concentrations were tested for each metabolite, typically 1 mM and 10 mM (**Tables S1 and S2**). The high metabolite concentrations were intended to mimic the spikes that occur during environmental shifts and perturbations, which may require rapid regulation of enzyme activity.

To compare metabolite-protein interactions between species, we extracted a list of all proteins affected by any metabolite for each strain and grouped them according to KEGG orthology groups (KOGs), including only orthology groups present in all four strains (**Figure S7**)**.** Principal component analysis (PCA) was used to cluster and compare metabolite-KOG interaction patterns between the species. Few interactions were detected at the low metabolite concentrations, which resulted in a relatively weak separation across species (**Figure S8-9**). However, larger differences between species were observed at the high concentrations (**Figure 3**). For GAP, a metabolite with more than 200 KOG interactions in all four species, interactions in the photoautotrophs clustered apart from those in the chemoautotrophs. Also G6P, the entering metabolite of the pentose phosphate (PP) and the Entner-Doudoroff (ED) pathway, showed a relatively high number of interactions in *Cupriavidus* that clustered apart from other species. Some metabolite-KOG interactions were similar in all species. For example, similarity of interactions with metabolites in lower glycolysis and in the reductive branch of the tricarboxylic acid cycle (2OG, PEP and citrate) may indicate conserved regulatory mechanisms in all species.

Interactions with AcCoA, ATP, citrate, and GTP were widespread in all four microbes (**Figure 3**). ATP, citrate and GTP are strong Mg^{2+} chelators(Mg^{2+} affinity ($\log_{10}K$) 4.1, 3.4, 4.1, respectively (Martell and Smith, 2013; Pecoraro et al, 1984)) and may sequester this common metal ion ligand from proteins in extracts, inducing conformational changes not caused by direct interactions with the metabolites. Indeed, the number of ATP interactions in *Synechocystis* extracts was reduced from 172 to 19 when the Mg^{2+} concentration in the LiP buffer was set higher than the ATP concentration (**Figure S10**).

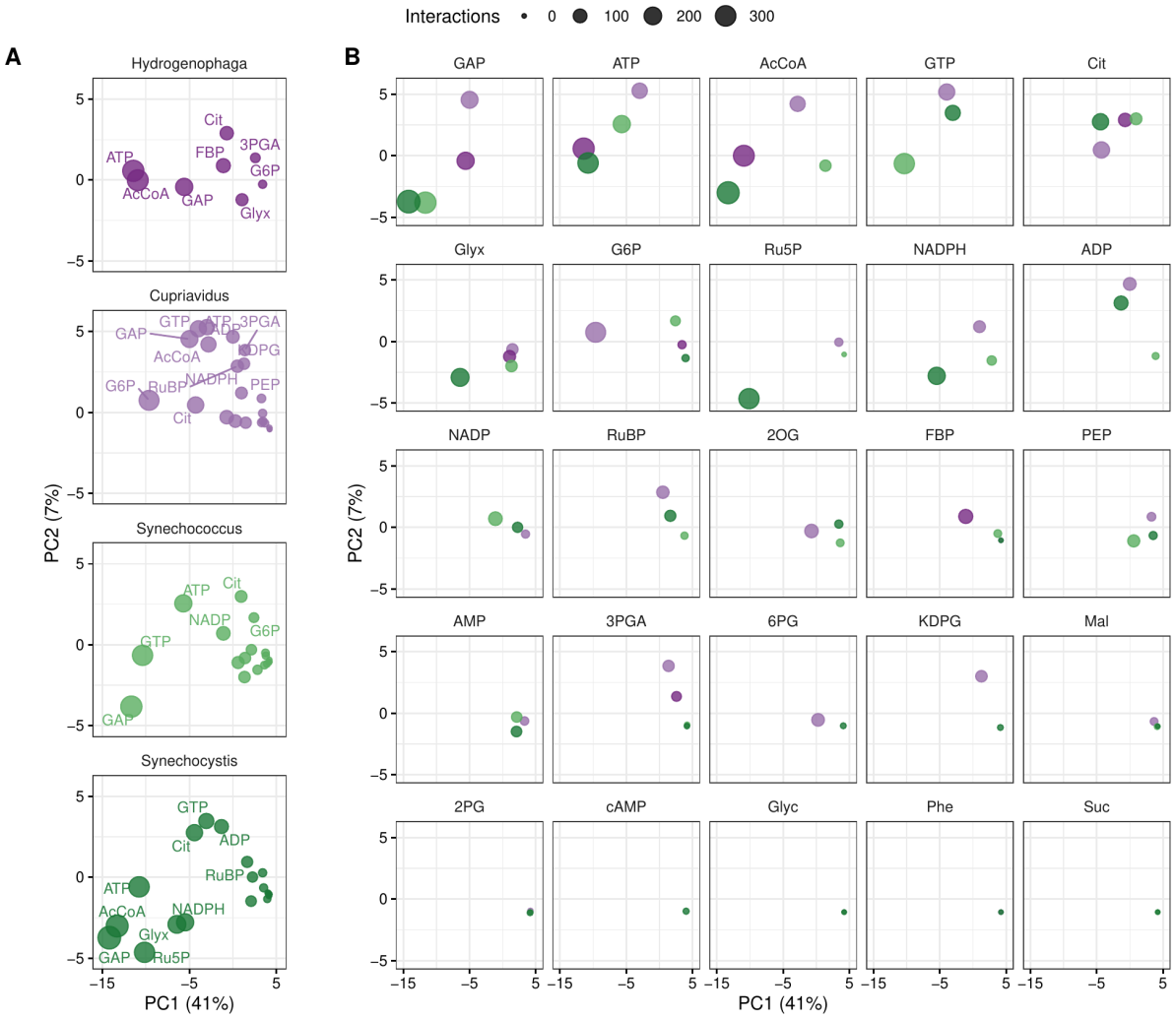

Figure 3. Similarity of ortholog interaction patterns, high added metabolite concentration. Principal components were calculated from the presence or absence of interaction with each of 477 orthologs (see Materials and Methods). All data points shown here are from the same principal component analysis, but split per organism (A) or metabolite (B) to reduce overplotting. Percentages indicate the fraction of the total variance captured by the principal components.

We next focused on interactions with enzymes of the Calvin cycle and major pathways that siphon carbon out of the cycle (**Figure 4**, high concentrations; **Figure S8,** low concentrations). Calvin cycle enzymes in these four microbes are phylogenetically diverse, though the cyanobacteria enzymes are more closely related than to the chemoautotroph orthologs (**Figure S11**). Some metabolite interactions were specific to certain species. For example, the photorespiratory intermediate glyoxylate showed extensive interactions in *Synechocystis,* even at low concentrations. Some “sink,” reactions, such as phosphoglucomutase (GPM) and ADP-glucose pyrophosphorylase (AGPase), involved in glycogen synthesis, had significantly more interactions in *Synechocystis* and *Synechococcus* than in the chemoautotrophs. In contrast, *Cupriavidus* Calvin cycle enzymes were particularly sensitive to intermediates of the PP and ED pathways, such as 6PG, G6P, and KDPG, as well as 2OG and RuBP. 3-Deoxy-D-arabinoheptulosonate 7-phosphate synthase

(DAHPS), an enzyme that reacts with E4P in the shikimate synthesis pathway, showed interactions with several metabolites primarily in *Cupriavidus,* at both high and low concentrations. In summary, while there were some interactions observed in all species, primarily AcCoA, ATP and GAP, most metabolites showed species-specific interactions with Calvin cycle enzymes.

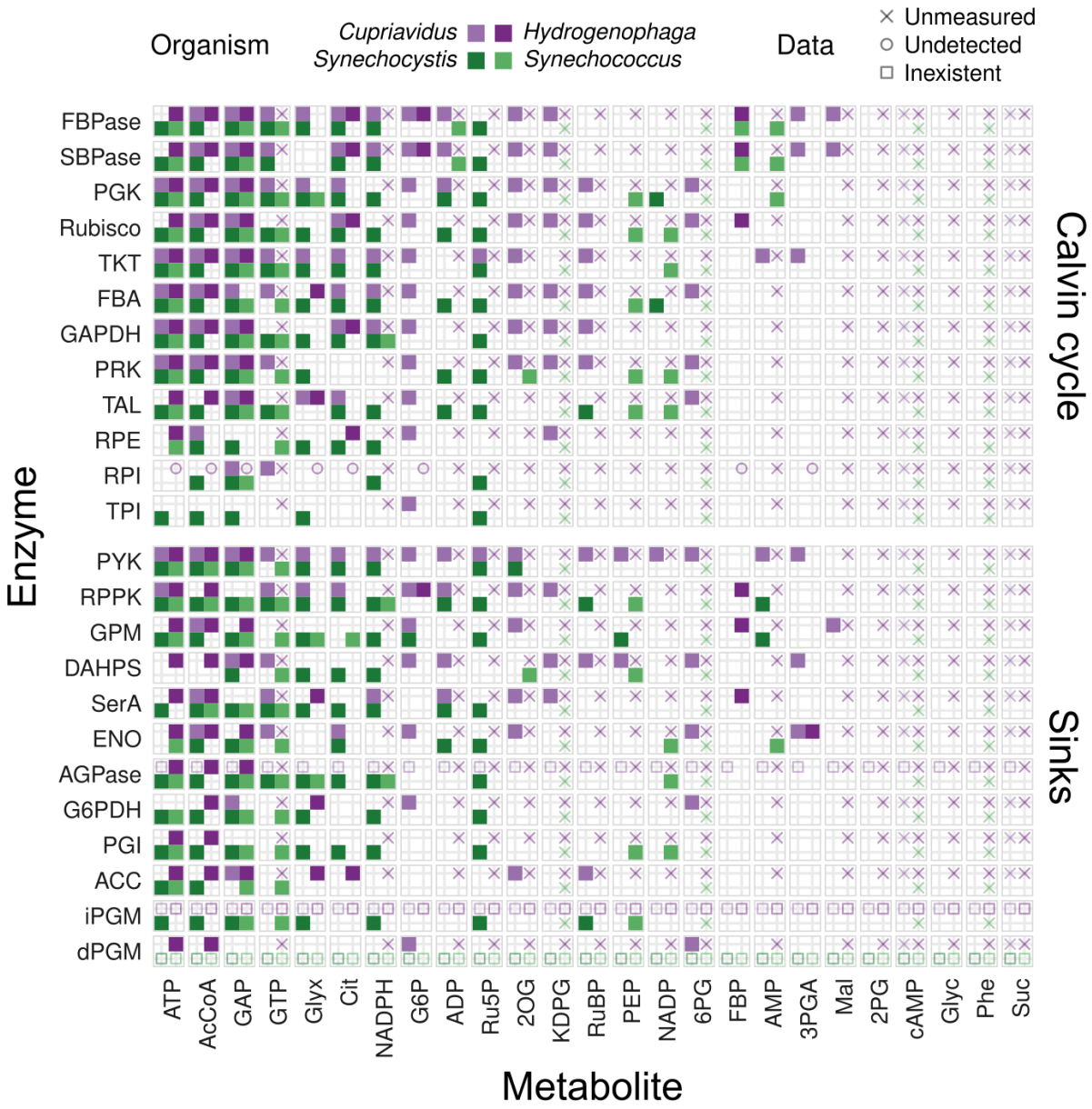

Figure 4. Interactions of Calvin cycle enzymes and selected central carbon metabolism enzymes with metabolites, high added metabolite concentration. Interactions between metabolites (columns) at high concentration and enzymes (rows) identified by KEGG EC number annotation are shown for each organism by tiles filled with the corresponding color. A blank tile indicates that the interaction was not detected, while missing protein data is explained by a symbol. A cross indicates that the particular condition was not measured, a circle indicates that the protein was not detected, and a square

indicates that there was no such enzyme in the corresponding genome. See **Figure S8** for interactions at low metabolite concentrations.

Validation of metabolite interactions and effect on enzyme activity

An interaction detected by LiP-SMap does not necessarily mean that the metabolite interacts directly, or that catalytic activity is affected. To explore whether metabolite-enzyme interactions identified by LiP-SMap tended to affect catalytic activity, we purified and assayed F/SBPase and transketolase from *Synechocystis* (*fbpI, tktA*) and *Cupriavidus* (*fbp3, cbbTP*). F/SBPase appears to have significant control over the overall rate of CO_2 fixation by the Calvin cycle in cyanobacteria (De Porcellinis et al. 2018; Liang and Lindblad 2016), as well as in the RuMP pathway (Stolzenberger et al., 2013; Woolston et al., 2018)). Transketolase catalyzes the transfer of a two-carbon ketol group to an aldehyde and connects metabolic flux in the Embden-Meyerhof-Parnas (EMP) pathway with the PP pathway and the regenerative part of the Calvin cycle. The transketolase of *E. coli* forms a dimer and exhibits considerable cooperativity between monomers (Wilkinson and Dalby, 2020). The transketolases of *Synechocystis* and *Cupravidus* have not been characterized previously.

Metabolites that altered the LiP of *Synechocystis* F/SBPase (syn-F/SBPase) and *Cupriavidus* F/SBPase (cn-F/SBPase) were screened for effects on kinetics and for direct binding by thermal shift assay (melting temperature (T_m) determination; **Table 1, Table S3**). GAP (0.5 mM) stimulated syn-F/SBPase and cn-F/SBPase activity by reducing the K_M value (**Figure 5**). Syn-F/SBPase was also activated by lower GAP concentrations (0.05 and 0.15 mM), while the GAP isomer dihydroxyacetone phosphate (DHAP) did not have an effect at concentrations up to 0.2 mM (**Figure S16**). GAP also caused a thermal shift of the syn-F/SBPase enzyme at multiple Mg^{2+} concentrations, indicating that altered LiP and kinetics are caused by a direct conformational change mediated by GAP, and that the effect is not due to sequestration of the required Mg^{2+} cofactor from the enzyme (**Figure S17**). In contrast, no thermal shift was observed upon adding GAP to cn-F/SBPase (**Figure S13**). Addition of NADPH at 3 mM reduced the maximum rate of both syn-F/SBPase and cn-F/SBPase up to 35%, but inhibition was not significant at substrate concentrations below K_M (**Figure 5**). The NADPH effect was relatively weak, as 1 mM NADPH reduced the maximum rate of syn-F/SBPase by 10% (**Figure S15**). NADPH Increased the thermal stability of cn-F/SBPase but not syn-F/SBPase (**Figure S13-14**). The similar kinetic effects of NADPH and GAP on both F/SBPase variants suggest evolutionary conservation, as syn-F/SBPase (class II) and cn-F/SBPase (class I) have similar folds but little sequence similarity (Brown et al., 2009; Feng et al., 2014a).

Citrate at 5 mM reduced the substrate affinity of syn-F/SBPase (**Figure S18**), which is consistent with the presence of citrate in the crystal structure of *Mycobacterium* F/SBPase, as well as citrate sensitivity of that enzyme (Wolf et al., 2018). However, thermal shift assays indicated that the inhibitory effect of citrate was likely due to chelation of Mg^{2+} from the active site of F/SBPase (**Figure S19**).

We also tested enzyme sensitivity to AMP, a known inhibitor of syn-F/SBPase (IC_{50} = 34 μM (Feng et al., 2014a)), although AMP did not show a LiP-SMap interaction with either

enzyme. Due to the strong binding of AMP to syn-F/SBPase, it is possible that residual AMP in proteome extracts after washing may mask conformational changes from externally added AMP. The *Synechococcus* PCC 7942 F/SBPase, which is less sensitive to AMP inhibition (IC50 = 260 µM (Tamoi et al., 1996)), did show an interaction with AMP. Addition of 0.25 mM AMP completely inhibited syn-F/SBPase activity, whereas cn-F/SBPase was relatively insensitive (**Figure 5, Figure S12**). AMP increased the thermal stability of both enzymes, indicating a direct metabolite interaction and conformational change (**Figure S13-14**). In contrast, ADP (1 mM) had a much smaller impact on syn-F/SBPase activity (20% decrease, **Figure S15**). ATP did not significantly alter the T_M of either syn-F/SBPase nor cn-F/SBPase (**Figure S13-14**).

Table 1. Validation of LiP-SMap metabolite interactions with F/SBPase *in vitro.* Changes in kinetic parameters were determined by enzyme kinetic assays (**Figure 5, Figure S18, Table S3**). The kinetic effect of a metabolite was considered significant for $p < 0.05$ (comparing kinetic parameters) and >20% change in rate for at least two tested substrate concentrations. Changes in melting temperature (T_m) greater than 2 °C were considered significant.

Effector (mM)	**LiP-SMap interaction**	**Kinetics change**	**T_m change**
syn-F/SBPase			
AcCoA (2)	Yes	Not significant	Not significant
AMP (0.25)	No	-k_{cat}	Increase
Citrate (5)	Yes	+K_M	Decrease
GAP (0.5)	Yes	-K_M	Increase
NADPH (3)	Yes	-k_{cat}, n_H	Not significant
cn-F/SBPase			
AMP (0.25)	No	Not significant*	Increase
GAP (0.5)	Yes	-K_m	Not significant
NADPH (3)	Yes	-k_{cat}, -K_M	Increase

*5 mM AMP reduced reaction rate ~40% (p-value = 0.002) at saturating substrate concentration (300 µM FBP), see **Figure S12**. n_H: Hill coefficient.

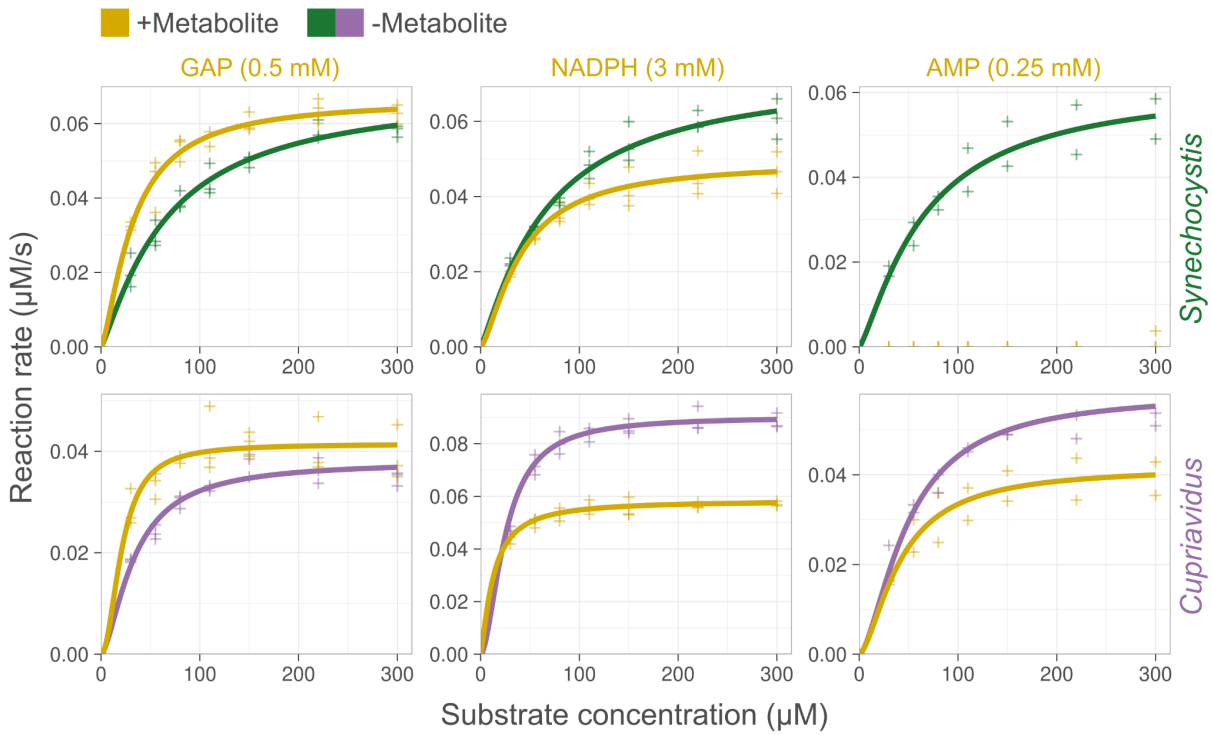

Figure 5. Effect of selected metabolites on the activity of *Synechocystis* and *Cupriavidus* F/SBPase *in vitro*. Reaction rates were measured at different substrate concentrations (FBP) in duplicates or triplicates (crosses). Lines represent data fit to the Hill equation. No catalytic activity was detected for syn-F/SBPase treated with AMP. Plots for other tested metabolites are shown in **Figure S18**.

The peptide resolution of LiP-SMap data indicated that GAP and NADPH affect syn-F/SBPase at sites that are distinct from the AMP allosteric site (**Figure 6**). We created a single amino acid exchange variant of syn-F/SBPase (R194H). This amino acid is located at the enzyme surface in a β-sheet that connects the substrate-binding site to the AMP-binding site. This mutant lost AMP sensitivity, but retained sensitivity to both GAP activation and NADPH inhibition (**Figure S20, Figure S12**).

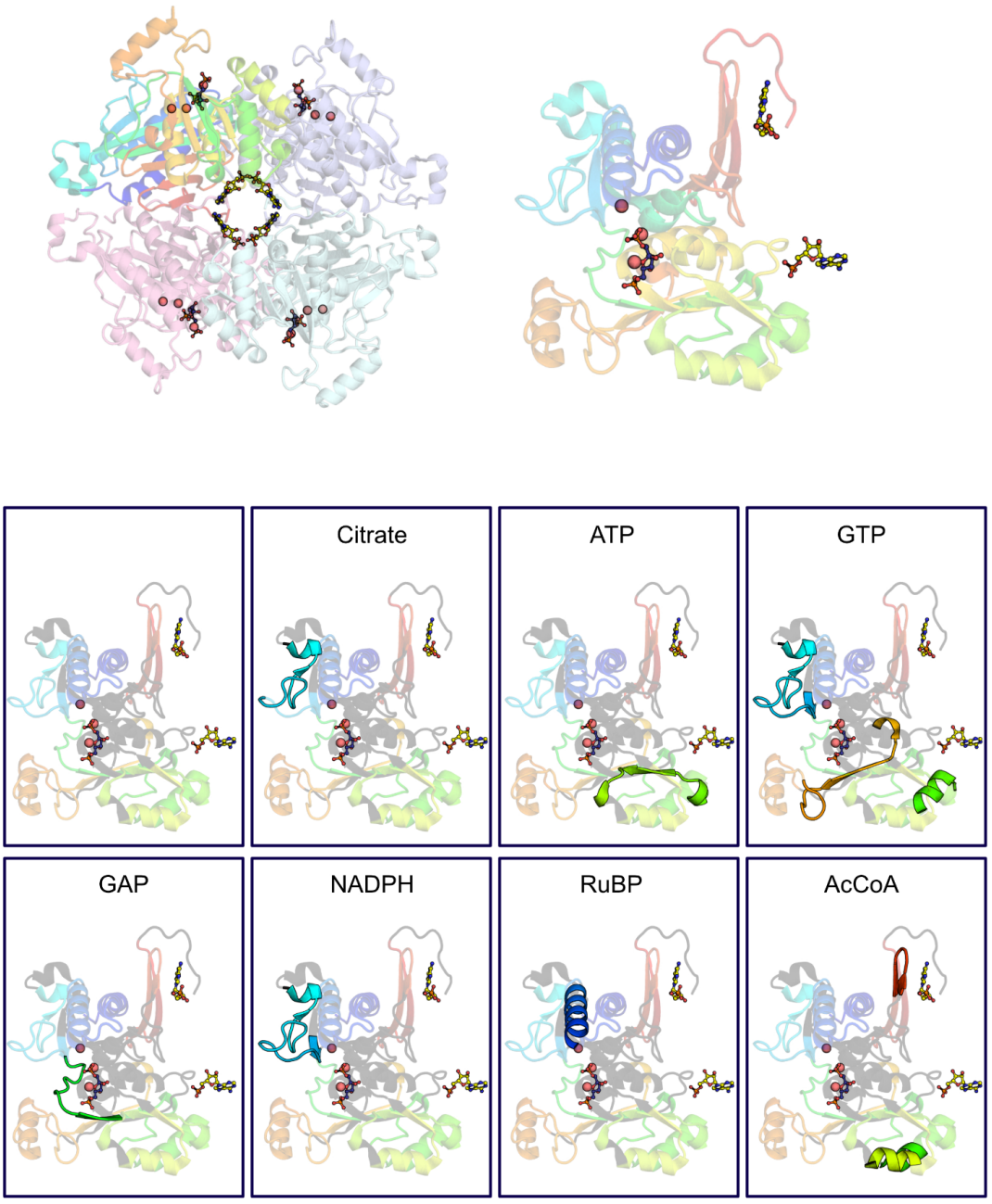

Figure 6. Structure of *Synechocystis* F/SBPase showing peptide coverage and affected peptides from LiP-SMap. Top left: F/SBPase assembles as a homotetramer (PDB-ID: 3RPL (Feng et al., 2014a)). The substrate FBP (shown as blue sticks) is coordinated by active site residues as well as Mg^{2+} ions (red spheres). AMP allosteric inhibitor molecules are located in the central interface of the tetramer (yellow sticks). Top right: monomeric view colored according to different structural elements, showing interaction with FBP and the AMP molecules at two adjacent interfaces with other monomers. Bottom: Monomeric view as shown in top right panel with peptides that were not detected in any condition shown as dark-gray ribbons. Peptides affected by the indicated metabolites (high added concentration) are outlined as opaque ribbons in individual panels.

The transketolases syn-TKT and cn-TKT were screened *in vitro* against all metabolites that showed a LiP-SMap interaction with the enzyme in any of the four species (**Table S4**). The most prominent effect was from AMP and DHAP, which reduced the activity of syn-TKT and cn-TKT, respectively. While ATP and ADP inhibition of transketolases have been shown (Markert et al., 2014), inhibition by AMP has not been reported. Addition of many other metabolites also affected transketolase activity, but the effects were small (< 20% change in rate; **Figure S21-22, Table S4**). None of the tested metabolites had a significant effect on the thermal stability, although a slight thermal shift was observed upon addition of G6P to cn-TKT (**Figure S23**). The results of these assays show that interactions detected by LiP-SMap are not always relevant for catalysis.

Predicted effects of enzyme-metabolite interactions on flux control in *Synechocystis*

We next evaluated the effects of the validated F/SBPase interactions in terms of flux control using an expanded kinetic model of central metabolism (Janasch et al., 2019). Two model variants were considered, a “base model” and a model with added F/SBPase regulations (“Base” and “FSBPase”, respectively; **Figure 7A**). For each model variant, we examined stability and flux control coefficients. This entailed generating a large set of possible metabolic states, defined by metabolic fluxes, metabolite concentrations, and enzyme kinetic parameters. First, a single set of steady-state fluxes was calculated, assuming nutrient-replete autotrophic growth. Then, 5000 sets of feasible metabolite concentrations that result in a positive driving force through each reaction step were randomly generated. For each metabolite set, 1000 sets of kinetic parameters (V_{max}, K_M, K_i, K_a) were randomly sampled in a space constrained by metabolite concentrations and metabolic fluxes. The two resulting model ensembles (5 million models each) were used to assess and compare both metabolic models in terms of flux control and stability.

As a first analysis step, the system stability in both models was compared. Here, stability refers to the ability of the system to return to its metabolic state upon an infinitesimal small perturbation of the metabolite concentrations. Generated parameter sets in the “Base” model had a median stability of 38% over all metabolomes (min 11%, max 58%), compared to 67% for the original Calvin cycle model (min 25%, max 93%; (Janasch et al., 2019)). The lower stability was not surprising as expanding the system out from the intrinsically stable Calvin cycle provides more potential for components to influence stability. The addition of regulation on F/SBPase did not alter stability significantly (model “FSBPase” median: 40%, min: 11%, max: 60%). The sampling of thermodynamically feasible metabolomes and the subsequent analysis of the dynamics around the steady-state allows for the association of metabolite concentrations with stability (**Figure S24).** Higher concentrations of the Rubisco-substrate RuBP are linked to instability in both model variants, albeit less pronounced than in the original analysis of the isolated Calvin cycle (Janasch et al. 2019). The distributions of metabolite concentrations in stable and unstable states was similar in the Base and FSBPase models; the added regulations on F/SBPase did not appear to affect system stability.

Fully parameterized kinetic models enable the quantification of flux control using metabolic control analysis (MCA), resulting in flux control coefficients (FCCs) for each reaction over every other reaction ("effectors," and "targets,"; **Figure 7B**, **Figure S25** for all FCCs). The supply of ATP and NADPH via the light reactions, and orthophosphate showed high FCCs for most other reactions. Furthermore, PRK had a positive FCC for many reactions, while RubisC (carboxylation reaction of Rubisco) had positive FCCs only over reactions downstream of the Calvin cycle towards the TCA cycle. Flux control for an enzyme was often local, only over other enzymes in the pathway or subnetwork. ALD and F/SBPase were among the most affected reactions. This is likely because their low steady-state fluxes (Gopalakrishnan et al., 2018) make them highly sensitive, resulting in relatively large FCCs. Trends in FCCs were similar in the Base and FBPase models, with some distinctions (**Figure 7C**, **Figure S26**). In the FSBpase model, FCCs of some reactions changed sign, but most of these were close to 0. The FCCs affecting ALD, FBPase and PYK were among the most amplified in the FSBPase model. The increased magnitude of the FCCs means a higher sensitivity of these target reactions to effector reactions. For example, NADPase has a higher (negative) FCC for FBPase and ALD reactions, reflecting the impact of the added inhibition of FBPase by NADPH. The enhanced sensitivity of PYK upon addition of F/SBPase regulations may be because the F/SBPase substrate FBP is an allosteric activator of PYK. The F/SBPase reaction itself had only slight changes in its FCC over other reactions.

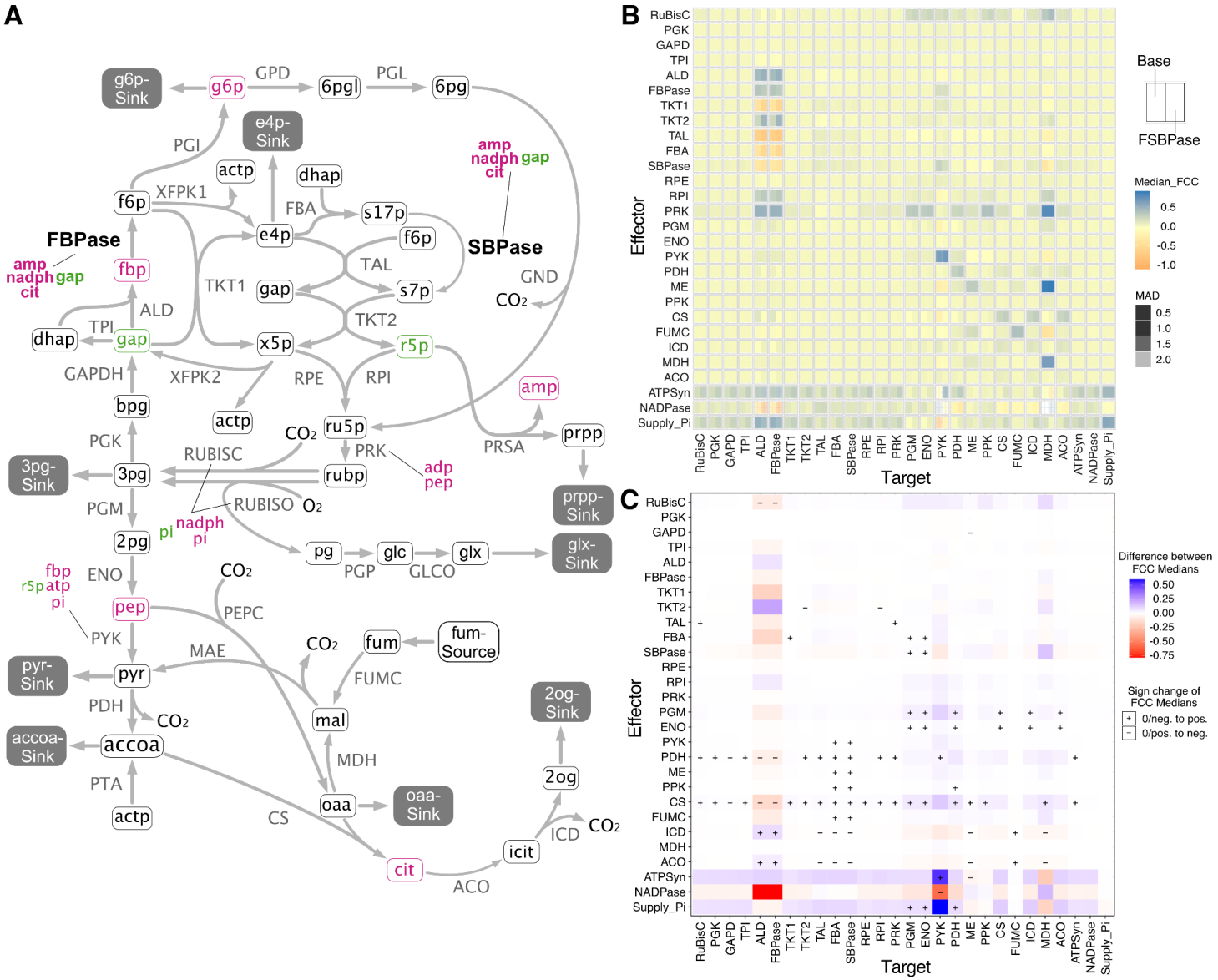

Figure 7. Regulations on F/SBPase in the context of metabolism and flux control. A) Schematic overview of the modeled metabolism showing all included biochemical regulations. F/SBpase interactions are included only in the F/SBPase model. Red: inhibition, Green: activation. B) Median flux control coefficients (FCCs) and median absolute deviation (MAD) over the whole model ensemble for both model variants. C) Difference between medians of FCCs between model variants. +/- indicate if the median FCC changed sign.

Discussion

The chemoproteomic workflow LiP-SMap was applied to reveal new metabolite-level regulation of enzymes within the Calvin cycle and central carbon metabolism, comparing four autotrophic bacteria. The importance of metabolite-level regulation is high for applied biotechnology. For example, it was recently shown that the photorespiratory metabolite 2PG

acts as a feedback inhibitor of the Calvin cycle in *Arabidopsis thaliana* by inhibiting TPI and SBPase at sub-millimolar, biologically relevant concentrations (Flügel et al., 2017). An AMP-insensitive variant of the *E. col* FBPase was used to increase starch production from formate in a recently reported *in vitro* enzyme cascade (Cai et al., 2021). In the context of such works, LiP-SMap could aid in finding new regulators and guide protein engineering.

We found that some tested metabolites interacted extensively in all organisms, such as ATP, GTP, GAP, AcCoA, and citrate. However, most metabolites showed species-specific interaction patterns, which could indicate the importance of these as metabolic signals and regulators in relation to a certain metabolic capacity or evolutionary adaptation. The extent of interactions at low added metabolite concentrations (0.5-1 mM) was significantly less than at high concentrations (5-10 mM). Metabolite control of enzyme activity is therefore likely not prevalent at steady state *in vivo* concentrations (< 1 mM), but rather when metabolite levels fluctuate or spike, such as during environmental shifts or when new metabolic pathways are installed (Kopka et al., 2017).

GAP interacted with a high number of proteins in all species, which suggest that post-translational regulation and signaling by GAP could be relevant for optimal and stable flux in central metabolism in general. Clustering analysis showed that a subset of GAP interactions in the photoautotrophs were different than in the chemoautotrophs. GAP intersects several central pathways, such as EMP, ED, PP and the Calvin cycle, and different utilization of these pathways between species may require specific regulation by GAP. Variability in the abundance of GAP could potentially regulate anaplerotic flux through the ED, PP and PGI shunt to balance and stabilize Calvin cycle flux (Makowka et al., 2020). In contrast, the ED pathway in *Cupriavidus* is the main route of fructose catabolism, whereas the EMP pathway is inactive (Alagesan et al., 2018). The preferred usage of the ED pathway to catabolize fructose could also explain why G6P, the entering metabolite of the ED pathway, showed significantly more interactions with *Cupriavidus* enzymes within the Calvin cycle and PP pathway. Hypothetically, G6P may signal the availability of fructose in the growth environment and play a role in the activation of sugar catabolism. The ED pathway metabolite KDGP may also act as a post-translational regulator in *Cupriavidus*, as it was found to interact more with *Cuprivavidus* enzymes.

Enzymes in glycogen synthesis, phosphoglucomutase (GPM) and ADP-glucose pyrophosphorylase (AGPase), showed more interactions in *Synechocystis* and *Synechococcus* compared to the chemoautotrophs. Distinct regulation of glycogen metabolism in *Cupriavidus* could be expected, as glycogen is synthesized from maltose-phosphate rather than ADP-glucose (Löwe et al., 2021). The photorespiration metabolite glyoxylate interacted with both GPM and AGPase in the two cyanobacteria, which suggests that elevated levels of glyoxylate in response to inorganic carbon limitation may participate in the associated activation of glycogen degradation (Eisenhut et al., 2007, 2008), though we did not test this. The GPM enzyme is potentially regulated by thioredoxin in *Synechocystis* (Lindahl and Kieselbach, 2009), as well as by phosphorylation (Doello et al., 2021). Therefore, rapid post-translational regulation of glycogen metabolism appears to be an important feature of photoautotrophic metabolism.

Validation of LiP-SMap-detected metabolite interactions with *Synechocystis* and *Cupriavidus* F/SBPase showed that GAP activates both enzymes. Such feed-forward activation may work to prevent excessive GAP accumulation and increase Calvin cycle flux in response to up-shifts in light and CO_2 levels in the growth environment. Feed-forward regulation in glycolysis and gluconeogenesis has been reported. In *E. coli* and red blood cells, pyruvate kinase is stimulated by the glycolysis intermediate FBP (Kochanowski et al., 2013; Schuster and Holzhütter, 1995). The type I FBPase in *E. coli* is stimulated by the gluconeogenic substrate PYR (Hines et al., 2006; Link et al., 2013). In photosynthetic microbes, intracellular levels of GAP, DHAP, FBP and SBP fluctuate with light, changing more than ten-fold in the microalgae *Chlamydomonas reinhardtii* when shifted from darkness to light (Mettler 2014). *Synechocystis* grown in a day-night regime show increased levels of Calvin cycle intermediates during the day, which correlates with light intensity, growth rate and Calvin cycle flux (Werner 2019, Jaiswal & Wangikar 2020). Thus, feed-forward activation of F/SBPase by GAP may provide fitness in terms of faster growth and CO_2 fixation rates during rich light and CO_2 conditions. Although the kinetic model revealed the influence of added regulation of F/SBPase on flux control of many reactions, direct influence of the feed-forward activation by GAP was not captured by this approach. The impact of such regulatory interactions could be masked by the broad sampling range of kinetic parameters and metabolite concentrations, which in turn could be refined by incorporating additional experimental data (metabolomics and proteomics) and simulating multiple metabolic states as well as dynamic changes between them.

Both syn-F/SBPase and cn-F/SBPase were inhibited by NADPH at 3 mM, a concentration considerably higher than reported *in vivo* values (~200 µM, Table S1). Intracellular NADPH levels will accumulate if production from the light reactions are greater than the consumption by metabolic processes, which could occur in response to sudden shifts in light and nutrient availability (Hauf et al., 2013; Holland et al., 2015; Tanaka et al., 2021). The syn-F/SBPase is strongly activated by DTT *in vitro* by the disruption of disulfide bonds in its structure, which is presumably mediated by reduced thioredoxin *in vivo* (Feng et al., 2014a). The relatively weak inhibitory effect at high NADPH could be a fine-tuning regulatory mechanism to rapidly reduce flux in the Calvin cycle and/or in glycogen synthesis upon sudden nutrient depletion or metabolic perturbation. However, to determine the relevance of this regulation on autotrophic metabolism, mutational studies or dynamic metabolic modeling is required.

The inhibition of syn-F/SBPase by AMP has been reported previously, though its role in Calvin cycle regulation is not clear (Feng et al., 2014a). AMP levels have been shown to increase above $K_{i,\,AMP}$ during the first 30 minutes of carbon limitation, which would be expected to inactivate F/SBPase and the Calvin cycle (Selim et al., 2018). Post-translational inactivation of F/SBPase could facilitate a rapid downregulation of the Calvin cycle in the early response to carbon limitation, and enable the mobilization of glycogen via the pentose phosphate pathway towards TCA cycle intermediates. Replenishment of TCA cycle intermediates is important for sustained amino acid synthesis that supports 2PG detoxification via the C2 cycle (Eisenhut et al., 2008). Cn-F/SBPase was considerably less sensitive to AMP. The proposed involvement of AMP-inhibited syn-F/SBPase during inorganic carbon limitation is presumably less relevant in *Cupriavidus*, since this bacterium can utilize a range of organic carbon substrates in its soil habitat (Park et al., 2011).

Interactions detected by LiP-SMap are not always direct, but can arise from secondary effects of metabolite addition, such as Mg^{2+} chelation. Metabolite chelation of Mg^{2+} ions likely explains the high number of interactions observed for e.g. ATP, GTP, and citrate. Wide-spread interactions detected for GAP could be due to its reactivity as an aldehyde, since glyceraldehyde has been shown to form Schiff-base adducts with lysine residues on carbonmonoxyhemoglobin *in vitro* (Acharya and Manning, 1980). However, covalent modification on proteins by GAP has not been reported. Indirect effects may also occur from enzymatic conversion of the metabolite, although the removal of endogenous cofactors from the proteome extracts by filtration is presumed to limit such effects. Even though secondary effects could be confounding, they may still be relevant for metabolism *in vivo.* For example, excessive accumulation of citrate and ATP, which could occur during nitrogen depletion, may inactivate ribosomes and anabolic processes. Mg^{2+} sequestration is particularly relevant for photosynthetic organisms, as Mg^{2+} levels change significantly over light dark cycles (Farhat et al., 2016; Li et al., 2020).

By quantification of individual peptides, the LiP-SMap method can provide insight into the binding mode of metabolites to a protein, which is an extra level of information compared to inference methods. In this respect, it may work best in tandem with other interaction-proteomics techniques, such as thermal proteome profiling. Such information is relevant for protein engineering strategies that seek to alter the regulatory effect of the interaction. We demonstrated the usefulness of peptide-level data by creating an AMP-insensitive *Synechocystis* F/SBPase mutant with retained NADPH and GAP sensitivity, by the replacement of an amino acid distant from peptides interacting with NADPH and GAP.

The qualitative assessment of the presented LiP-SMap dataset showed that the method is capable of detecting and screening for novel metabolite-protein interactions in proteome extracts. However, the method's sensitivity to detect existing interactions is limited by the peptide coverage from MS. Peptide coverage could potentially be improved by optimizing the tryptic digestion, analyzing all samples in the same MS run, and a higher degree of chromatographic fractionation in the MS, though the latter will considerably increase the required MS resources. The false detection rate of the current method protocol is relatively high, as 36-74% of the interactions were not detected in repeated LiP-SMap experiments. Lower reproducibility was observed among proteins with a high peptide coverage, which is perhaps non-intuitive. The risk to falsely assign a protein as metabolite interacting increases with higher peptide coverage, since a single falsely assigned interacting peptide is sufficient to call the whole protein as interacting. It is therefore important to also improve the accuracy of peptide quantification, and not just peptide coverage. False detections can arise if peptides are not equally digested by proteinase K or trypsin in metabolite-treated samples compared to control samples. Random variations in peptide digestion are difficult to avoid due to the complexity of the protein extracts, comprising thousands of cleavage sites. A certain degree of error is furthermore inherent to peptide quantification by MS. The influence of random errors can be mitigated by generating a higher number of replicate pairs of metabolite-treated and control peptide digests. Ideally, these should be generated from separate proteome extracts and at different occasions to overcome biases. Quantification of the effect of added metabolite over a broader concentration range can also increase confidence in a particular interaction (Piazza et al., 2020). Furthermore, the inclusion of a control that is not digested with proteinase K may improve the data quality because it

enables the quantification of LiP degradations rates, which is a more direct measure of a peptide's altered exposure after a conformational change.

Materials and methods

LiP-SMap experimental procedures

Cultivations and harvest

Cupriavidus necator strain DSMZ 428 was grown in Ralstonia Minimal Media (RMM) with 100 mM HEPES pH 7.5 under chemostat conditions in a Photon Systems Instruments Multi-Cultivator MC-1000 OD. Each reactor tube was set up to a volume of 55 mL, OD_{600} 0.05 and 3.5 g/L fructose. Once growth ceased, an inlet feed of 0.01 - 0.05 mL/min of 8 g/L formic acid in RMM with 100 mM HEPES pH 7.5 was initiated. Cultivations were kept running until a stable OD_{600} had been observed for at least 5 doubling times. *Hydrogenophaga* pseudoflava strain DSMZ 1084 were grown at 30 °C and 200 RPM in sealed flasks of ~135 mL containing ~25 mL DSMZ media 133 and ~110 mL of gas (70% H_2, 15% CO_2 and 15% O_2) at 1 bar overpressure. Cultivations were started from overnight pre-cultures grown on 1.5 g/L acetate and harvested during exponential growth at OD_{600} ~1.0. *Synechocystis sp*. PCC 6803 (gift from Klaas Hellingwerf, University Amsterdam) & *Synechococcus elongatus* PCC7942 (from Pasteur Culture Collection, France) were grown in BG-11 media at 1% CO_2 and a light intensity of ~70 $\mu mol \cdot s^{-1} \cdot m^{-2}$ in 500 mL flasks containing 100 mL liquid until an OD_{730} of ~1.0. For each microbe, four biological replicate cultivations were performed, and immediately before harvest the replicates were pooled. Cells were harvested by centrifugation and washed three times with cold lysis buffer before being resuspended in a small amount of lysis buffer, snap frozen in liquid nitrogen, and stored as aliquots in -80 °C. The cyanobacteria were exposed to light at ~ 400 $\mu mol \cdot s^{-1} \cdot m^{-2}$ for 5 minutes prior to snap freezing.

Proteome extraction

Frozen aliquots were thawed on ice and lysed mechanically through bead beating by a FastPrep-24 5G lysis machine over six cycles of 45 seconds at 6.5 m/s with 30 seconds on ice between cycles. The lysate was spun down and the supernatant was run through a Zeba Spin Desalting Column. Protein concentration in the desalted lysate was evaluated using a Bradford assay. The samples were kept at 4 °C throughout the procedure.

Limited proteolysis

For every experiment three sample groups were created, one with no added metabolite and two with different concentrations of metabolite specified in Table S1. Each sample group was prepared as four technical replicates with 1 µg/µL extracted protein. Proteinase K was simultaneously added to all samples at a 1:100 protease to protein ratio and incubated at 25 °C for exactly 10 minutes before immediate denaturation.

Complete digestion

The protein mix was incubated at 96 °C for 3 min prior to treatment with 5% Sodium Deoxycholate and 10 mM DTT and another 10 min at 96 °C after. The samples were then alkylated by 10 mM Iodoacetamide at RT for 30 min in the dark, after which proteases LysC and trypsin were applied at a 1:100 protease to protein ratio and incubated at 37 °C and 400

RPM in a thermocycler for 3 and 16 hours, respectively. Digestion was halted by addition of formic acid to reduce pH below 2 which caused sodium deoxycholate to precipitate. Samples were then centrifuged at 14,000g for 10 min after which the supernatant was removed and stored at -20 °C.

Peptide purification

Pipette tips packed with six layers of C18 matrix discs (20-200 µL; Empore SPE Discs) were activated with acetonitrile and equilibrated with 0.1% formic acid prior to being loaded with thawed peptide mixes. The matrix was then washed twice with one loading volume of 0.1% formic acid before being eluted with a mixture of 4:1 ratio of acetonitrile to 0.1% formic acid. The eluate was stored at -20 °C until analysis by LC-MS.

LC-MS analysis

Analysis was performed on a Q-exactive HF Hybrid Quadrupole-Orbitrap Mass Spectrometer coupled with an UltiMate 3000 RSLCnano System with an EASY-Spray ion source. 2 µL of each sample was loaded onto a C18 Acclaim PepMap 100 trap column (75 µm x 2 cm, 3 µm, 100 Å) with a flow rate of 7 µL per min, using 3% acetonitrile, 0.1% formic acid and 96.9% water as solvent. The samples were then separated on ES802 EASY-Spray PepMap RSLC C18 Column (75 µm x 25 cm, 2 µm, 100Å) with a flow rate of 0.7 µL per minute for 40 minutes using a linear gradient from 1% to 32% with 95% acetonitrile, 0.1% formic acid and 4.9% water as secondary solvent. After separation MS analysis was performed using one full scan (resolution 30,000 at 200 m/z, mass range 300-1200 m/z) followed by 30 MS2 DIA scans (resolution 30,000 at 200 m/z, mass range 350-1000 m/z) with an isolation window of 10 m/z. Precursor ion fragmentation was performed with high-energy collision-induced dissociation at an NCE of 26. The maximum injection times for the MS1 and MS2 were 105 ms and 55 ms respectively, and the automatic gain control was set to $3 \cdot 10^6$ and $1 \cdot 10^6$ respectively. The EncyclopeDIA and Prosit workflows were used to generate a predicted library from a fasta file of the appropriate organisms UniProt proteome set (*C. necator*: UP000008210, *Synechocystis sp.* PCC 6803: UP000001425, *Synechococcus elongatus sp*. PCC 7942: UP000002717, *H. pseudoflava*: UP000293912) against which an EncyclopeDIA search was performed to generate a list of detected peptides.

LiP-SMap data analysis

Peptides detected in at least three replicates in every sample group were tested for differential peptide abundance using the MSstats package (version 3.18.5) in R (version 3.6.3). For every peptide in each metabolite concentration comparison MSstats estimated fold changes and p-values adjusted for multiple hypothesis testing (Benjamini-Hochberg method) with a significance threshold of 0.01. A protein was considered to interact with a metabolite supplied at low or high concentration if at least one peptide showed significant interaction. General data and quality assessment statistics and visualizations were generated by the pipeline available at https://github.com/Asplund-Samuelsson/lipsmap, implemented in R version 4.1.1 with Tidyverse version 1.3.1.

Ortholog annotations

In order to compare metabolite-protein interaction patterns between organisms, it was necessary to determine orthologous genes. Ortholog labels from the eggNOG database were downloaded from UniProt (https://www.uniprot.org/) on 14 June 2021 for each protein

in the four organisms. Version 5.0 of eggNOG was used except for proteins Q31NB2 (ENOG4108VFZ), Q31RK3 (ENOG4105KVS), and Q31RK2 (ENOG4105HKE) in *Synechococcus*, which were annotated with eggNOG version 4.1. Only the 481 orthologs found in all organisms were considered. The number of interacting proteins were counted for each ortholog and metabolite concentration, in each organism. Furthermore, ortholog counts were summarized into the 20 functional categories each represented by a single letter, e.g. “A” for “RNA processing and modification.”

Principal component analysis of interactions with orthologs

The metabolite-protein interaction patterns of orthologs were compared between metabolites and organisms using R. The interaction per ortholog was first classified binarily so that the interaction was 1 (one) if there was at least one interaction for the ortholog in a particular combination of organism, metabolite, and concentration. Otherwise the interaction was classified as 0 (zero). Orthologs without interactions were filtered out. A matrix with rows representing organism and metabolite, and columns containing the binary interaction classification of each ortholog, was subjected to principal component analysis (PCA; function prcomp). The first two principal components were then plotted in order to visualize how similar different organisms and metabolites were in terms of interaction with the full set of orthologous genes. The PCA was performed separately for low and high metabolite concentrations.

Clustered heatmap of interactions with orthologs

The metabolite-protein interaction patterns of orthologs, summarized per ortholog functional category, were further inspected through visualization with a heatmap with clustered rows and columns. The ortholog interaction counts were normalized to indicate the fraction of interacting orthologs within each combination of functional category, organism, metabolite, and concentration. These fractions were then used to calculate Euclidean distance (function vegdist from library vegan) followed by clustering (ward.D2 method in function hclust), which determined the order of functional categories (heatmap rows), and metabolites and concentrations (heatmap columns). Organisms contributed both to row and column clustering. Finally, the ortholog interaction fractions were plotted as heatmaps, using row and column orders as described, with dendrograms clarifying the clustering (function ggtree from library ggtree).

Phylogenetic analysis

We wanted to compare evolutionary relationships of Calvin cycle proteins to their interaction patterns in the different organisms, prompting a phylogenetic analysis. Sequences for Calvin cycle KEGG orthologs (KO) in module M00165, supplemented with transaldolase (K00616 and K13810), triose-phosphate isomerase (K01803), and ribulose-phosphate epimerase (K01783), were downloaded from UniProt on 14 October 2021. Each set of KO sequences were reduced in number with cd-hit version 4.8.1 (Fu et al., 2012; Li and Godzik, 2006) by selecting the highest percent identity setting between 50% (-c 0.5) and 100% (-c 1), in 5% steps, that resulted in fewer than 1 000 representative sequences. For each KO set, we added any missing corresponding protein sequences in the four organisms studied here. Sequences were aligned using mafft version 7.453 at default settings (Katoh and Standley, 2013). The alignments were then used to construct phylogenetic trees with FastTree version 2.1.11 Double precision at default settings (Price et al., 2010). NCBI taxonomy data downloaded on 8 October 2021 was used to identify organism groups. Trees were plotted

using phytools and ggtree in R in order to visualize the phylogenetic distribution of sequences and metabolite interactions for the four organisms under study.
Ortholog analysis code is available at https://github.com/Asplund-Samuelsson/lipsmap.

Cloning and transformation

The tktA gene in *Synechocystis* PCC 6803 and the cbbTP gene in *C. necator* were PCR amplified using the primer pairs tktAF+tktAR and cbbTpF+cbbTpR respectively. The backbone pET-28a(+) was linearized using the primer pair pETF+peTR after which the constructs were assembled through Gibson assembly. The products were verified by sequencing and transformed into E. coli BL21 by heat shock.

tktAF: 5′-CCATTTGCTGTCCACCAGACAGTGAGGAGTTTTAAGCTTGG-3′
tktAR: 5′-CCGCGCGGCAGCCATATGAACATTATGGTCGTTGCTACCC-3′
cbbTpF: 5′-CCATTTGCTGTCCACCAGATCAAGCGTCCTCCAGCAG-3′
cbbTpR: 5′-CCGCGCGGCAGCCATATGGAGATGAACGCACCCGAACG-3′
pETF: 5′-CATATGGCTGCCGCGCGG-3′
pETR: 5′-CTGGTGGACAGCAAATGGGTCG-3′

Production and purification of recombinant F/SBPase and TKT

The mutants were cultivated in 2YT media at 37 °C and 200 RPM until OD 0.4-0.6 after which overexpression was induced by 1 mM IPTG. The tktA gene was incubated at 37 °C for 8h after induction, whereas the cbbTP gene was incubated at 18 °C for 24 hours. Cells were harvested by centrifugation at 4 °C and stored at -20 °C. Frozen pellets were resuspended in 3-5 mL of B-PER and incubated on a rocking table for ~30 min before centrifugation at 4,000 g. The soluble fraction was loaded onto an HisTrap Fast Flow Cytiva column (1 mL) and washed with wash buffer (50 mM Tris-HCl, 300 mM NaCl, 20 mM imidazole, pH 7.5) prior to elution with elution buffer (50 mM Tris-HCl, 300 mM NaCl, 500 mM imidazole, pH 7.5). Fractions containing transketolase were combined and the buffer was exchanged to storage buffer (50 mM Tris-HCl, pH 7.5) using a HiTrap Cytiva desalting column. The purified protein was quantified by Bradford assay and stored at -80 °C in aliquots.

Enzyme kinetic validation of TKT metabolite interactions

Transketolase was characterized following (Brilisauer et al., 2019). The conversion of D-ribose-5-phosphate and L-erythrulose to sedoheptulose-7-phosphate and glycolaldehyde was measured through the consumption of NADH by alcohol dehydrogenase when reducing glycolaldehyde to ethylene glycol. Initially, the kinetics were calculated from measurements of reaction rates at 12 different substrate concentrations (0, 100, 200, 300, 400, 500, 600, 800, 1000, 2000, 4000, 8000 µM) in quadruplicate. Subsequently, relative comparisons of enzyme kinetics were made as calculated from 8 different substrate concentrations (0, 100, 200, 500, 750, 1000, 2000 and 4000 µM) with and without 1 mM added metabolite. The tested metabolites were 2OG, 2PG, ATP, AMP, G6P, Citrate, Glyoxylate, Malate, NADP and DHAP. The reaction mix contained 100 mM glycylglycine buffer pH 7.5, 5 mM MgCl, 2 mM thiamine pyrophosphate, 0.5 mM NADH, 100 mM L-erythrulose, 10 U ADH, 2.875 µg/mL transketolase and D-ribose-5-phosphate to a final volume of 100 µL. Absorption was measured at 340 nm twice per minute over 30 minutes starting immediately after addition of D-ribose-5-phosphate.

Enzyme kinetic validation of F/SBPase metabolite interactions

To determine the effect of added metabolite on F/SBPase kinetic parameters, reaction rates were measured at eight different substrate concentrations (0, 30, 55, 80, 110, 150, 220, 300 µM) in the presence and absence of a metabolite (+M and -M). The conversion rate of FBP to F6P was determined from the release of inorganic phosphate over time, using a Malachite Green (MG) assay adapted from (Vardakou et al., 2014). MG dye stock (1.55 g/L Malachite Green oxalate salt, 3 M H_2SO_4) was used to prepare a fresh phosphate colorimetric development solution prior to each experiment (400 µL MG dye stock, 125 µL ammonium molybdate (60 mM), 10 µL Tween-20 (11% v/v)). The development solution was filtered through a 0.2 µm syringe filter and kept in the dark. Development plates were prepared by diluting 36 µL development solution in 100 µL buffer (50 mM Tris-Hcl, 15 mM $MgCl_2$) in each well. Enzyme solutions for +M and -M reaction conditions were prepared in two separate 8-tube PCR strips (VWR #732-1521 or low-protein binding) by mixing 25 µL reaction buffer, with or without metabolite (50 mM Tris-Hcl, 15 mM $MgCl_2$, 10 mM DTT, +M/-M), with 25 µL purified enzyme constituted in -M reaction buffer. The two strips were pre-incubated at 30 ºC for 12 minutes in a thermocycler together with two additional PCR strips containing substrate at eight different concentrations in -M reaction buffer. Reactions were initiated by quickly mixing 50 µL substrate with the enzyme mixture in one of the reaction strips (+M or -M), using a multipipette. The final enzyme concentration was 0.42 and 0.15 ng/µL for syn-F/SBPase and cn-F/SBPase, respectively. Reaction samples of 20 µL were immediately transferred and quenched in plate wells containing development solution wells before incubating the reaction strip at 30 °C. The initiation procedure was repeated for the second reaction strip with a two minute delay. Samples were collected after 10, 20, and 30 minutes after substrate addition. Each sampling event was followed by the addition of 7.5 µL sodium citrate (34% w/v) to stabilize the color of the development solution. Triplicate series of phosphate standards (0-100 µM) were added to each development plate as a reference. The plate was incubated for 20 minutes in the dark before measuring the absorbance at 620 nm in a plate reader. For kinetic assays testing a metabolite at different concentrations, the substrate concentration was either 60 µM (DHAP, GAP) or 300 µM (AMP, NADP), and reaction samples were collected at the zero and 10-minute timepoints. To quantify the amount of phosphate, background absorbance measured at time zero was first subtracted from raw absorbance measurements. Phosphate standard series were then used to convert absorbances to phosphate concentrations. Phosphate concentrations that were lower than 10 µM (sensitivity threshold) or that exceeded 60% of the initial substrate concentration (10-minute time points were always kept nonetheless) were removed. Reaction rates were calculated as the change in phosphate concentration over time using linear regression. To determine kinetic parameters, reaction rates and substrate concentrations were fit to the Hill equation using non-linear regression. A kinetic parameter (k_{cat}, K_M, n_H) change was considered significant if both $p < 0.05$ (Student's t-test) and a >20% change in rate was observed in at least two of the tested substrate concentrations.

Thermal solubility shift measurements

The samples were drawn up into capillaries and inserted in a Prometheus NT.48 nanoDSF machine set to 95% excitation power that assayed the stability of the sample while increasing the temperature from 20 °C to 95 °C at a rate of 1 °C per minute. Transketolase samples were prepared in 50 mM Tris-HCl pH 7.5 with 5 mM $MgCl_2$, 2 mM TPP, 200 ng/µL enzyme and 1 mM of metabolite. In addition, samples with and without 2 mM TPP and 10 mM DTT were also run to assay the effect of the cofactor and reductive power on protein stability. F/SBPase samples were prepared in 50 mM Tris-HCl pH 8 with 15 mM $MgCl_2$, 10

mM DTT and varying concentrations of metabolite (Table 1). The effect of GAP and citrate (0.5, and 5 mM, respectively) on syn-F/SBPase was analyzed at different $MgCl_2$ concentrations to test whether T_m changes were caused by magnesium chelation. T_m changes greater than 2 °C were considered significant.

Kinetic metabolic model

Model structure

The kinetic model for *Synechocystis* central carbon metabolism was based on a previous model (Janasch et al., 2019), and expanded to cover the reactions of photorespiration, oxidative pentose phosphate (OPP) pathway, anaplerotic reactions around acetyl-CoA and pyruvate, as well as the TCA cycle with its forked nature. The final model contained 53 reactions connecting 57 metabolites (41 internal). Sink reactions were formulated as irreversible Michaelis-Menten-type equations. Supply reactions followed mass action kinetics. Two model variants were created: One base model, including only the regulatory interactions in the previous version (Janasch et al., 2019), and one model with interactions on F/SBPase (AMP, GAP, NADPH, CIT).

Metabolic flux distribution

The steady-state flux distribution was obtained using a genome-scale metabolic model (GEM) of *Synechocystis* (Sarkar et al., 2019). All flux simulations were performed in Matlab R2020b using the Gurobi Optimizer version 9.1.1. First, the GEM was modified by allowing reversibility of the conversion of NADPH to NADH and replacing the two individual reactions corresponding to Rubisco carboxylase and oxygenase by a single Rubisco reaction representing 97% carboxylase and 3% oxygenase activity as implemented in a previous network reconstruction (Knoop et al., 2013). Flux were constrained by ranges taken from Gopalakrishan et al., 2018 (Gopalakrishnan et al., 2018), bicarbonate uptake was constrained to a maximum of 3.7 $mmol \cdot gDW^{-1} \cdot h^{-1}$ (Nogales et al., 2012). Maximizing autotrophic growth was set as the objective function and fluxes were sampled using the randomSampling function of the RAVEN Toolbox 2 version 2.4.3 (Wang et al., 2018) allowing for 95% of the optimized objective value. Fluxes were manually curated to adjust the genome-scale flux distribution to the small-scale kinetic model structure and transformed into mM/min by multiplying with a cellular density of 434.78 g/L (E. coli, (Bennett et al., 2008)).

Metabolite concentrations

Due to the uncertainty associated with published metabolomics datasets, potential thermodynamically feasible metabolite concentrations describing the metabolic state were randomly sampled, as performed similarly before (Janasch et al., 2019). Metabolite concentration ranges identified via NET analysis (Asplund-Samuelsson et al., 2018) were adjusted to the present model structure and used as constraints for the sampling. To cover the whole feasible solution space efficiently, a hit-and-run algorithm was employed. Starting from a feasible metabolite concentration set (fMCS), the algorithm randomly selects a direction and feasible step length to move through the logarithmic solution space, creating fMCSs with each step. MDF (Noor et al., 2014) analysis followed by thermodynamic variability analysis (Janasch et al., 2021 manuscript) was used to identify 83 fMCSs as starting points for the random sampling. For each initial fMCS, five runs were performed with each $1 \cdot 10^6$ steps, of which each 1000^{th} step was recorded resulting in ~415000 fMCSs. Pool sizes for the supply reactions were sampled in a range between 1.1x to 5x around their corresponding metabolite concentrations, simulating fast supply (pool size close to

metabolite concentration) and slow supply, respectively. For practical reasons 5000 fMCSs were randomly selected to form a representative overview of the thermodynamically feasible concentrations of the analyzed metabolic state to be used in the subsequent parameter sampling.

Parameter Sampling
Rate equations were generally parameterized around the corresponding metabolite concentrations by sampling the range of 0.01x to 100x metabolite concentration in logarithmic space for K_M values, corresponding to 99% to 1% active site saturation, as performed previously (Janasch et al., 2019). Inhibition constants K_i for the regulations identified by LiP-SMap were sampled in a narrower range of 0.2x to 5x around the metabolite concentrations used for the enzyme assays. For F/SBPase 50 µM, 3 mM and 5 mM were used for AMP, NADPH and CIT, respectively. For the activation of F/SBPase by GAP, K_m could maximally be reduced by 75%. Hill coefficients for FBPasewere sampled between 1 and 2, while for SBPase the range was between 1 and 4, following the observed difference between FBPase and SBPase reactions identified in (Feng et al., 2014a). V_{max} values were calculated back from metabolite concentrations, sampled kinetic constants and the steady-state flux distribution. For each of the 5000 fMCSs, 1000 parameter samplings were performed, resulting in an ensemble of 5 million kinetic steady-state models to be analyzed for stability and metabolic control.

Metabolic control analysis
The dynamic behavior of the models was analyzed by linearizing them around their steady-state as performed previously (Janasch et al., 2019; Murabito et al., 2014), based on (Reder, 1990), by forming the Jacobian matrix. The stability of each model in the ensemble was evaluated by calculating the eigenvalues of the Jacobian matrix, where positive eigenvalues cause instability. Flux control coefficients were calculated for all stable parameter sets based on elasticities and concentration control coefficients as described in (Janasch et al., 2019). The models and all code required to perform the kinetic modeling analysis is available at https://github.com/MJanasch/KX_Kinetics.

Acknowledgements

We are grateful to Michael Jahn (KTH Stockholm) for helpful discussion on proteomics and cultivation of *Cupriavidus necator*. We thank Ralf Steuer (Humboldt University, Berlin) for discussions on kinetic modeling.

Funding for this work was from the Novo Nordisk Foundation (grant numbers NNF19OC0057652 and NNF20OC0061469), the Swedish Research Council Vetenskapsrådet (grant number 2016-06160), and the Swedish Foundation for Strategic Research SSF (ARC19-0051).

Contributions
Conceptualization: JK, ES, PS, FE, IP, EPH
Experimental proteomics: JK, ES, DK, LS, FE
Proteomics data analysis: JAS, JK, ES, LS, FE

Enzyme kinetics and melting analyses: JK, KS, ES
Metabolic modeling: LZ, MJ
Writing initial draft: JK, ES, JAS, MJ, EPH
Editing of final draft: JK, ES, JAS, MJ, KS, EPH
Funding acquisition: PS, EPH

References

Acharya, A.S., and Manning, J.M. (1980). Reactivity of the amino groups of carbonmonoxyhemoglobin S with glyceraldehyde. J. Biol. Chem. *255*, 1406–1412.

Alagesan, S., Minton, N.P., and Malys, N. (2018). C-assisted metabolic flux analysis to investigate heterotrophic and mixotrophic metabolism in H16. Metabolomics *14*, 9.

Alliegro, M.C. (2000). Effects of dithiothreitol on protein activity unrelated to thiol-disulfide exchange: for consideration in the analysis of protein function with Cleland's reagent. Anal. Biochem. *282*, 102–106.

Asplund-Samuelsson, J., and Hudson, E.P. (2021). Wide range of metabolic adaptations to the acquisition of the Calvin cycle revealed by comparison of microbial genomes. PLoS Comput. Biol. *17*, e1008742.

Asplund-Samuelsson, J., Janasch, M., and Hudson, E.P. (2018). Thermodynamic analysis of computed pathways integrated into the metabolic networks of E. coli and Synechocystis reveals contrasting expansion potential. Metab. Eng. *45*, 223–236.

Barenholz, U., Davidi, D., Reznik, E., Bar-On, Y., Antonovsky, N., Noor, E., and Milo, R. (2017). Design principles of autocatalytic cycles constrain enzyme kinetics and force low substrate saturation at flux branch points. Elife *6*.

Beck, C., Knoop, H., Axmann, I.M., and Steuer, R. (2012). The diversity of cyanobacterial metabolism: genome analysis of multiple phototrophic microorganisms. BMC Genomics *13*, 1–17.

Bennett, B.D., Yuan, J., Kimball, E.H., and Rabinowitz, J.D. (2008). Absolute quantitation of intracellular metabolite concentrations by an isotope ratio-based approach. Nat. Protoc. *3*, 1299–1311.

Borirak, O., de Koning, L.J., van der Woude, A.D., Hoefsloot, H.C.J., Dekker, H.L., Roseboom, W., de Koster, C.G., and Hellingwerf, K.J. (2015). Quantitative proteomics analysis of an ethanol- and a lactate-producing mutant strain of Synechocystis sp. PCC6803. Biotechnol. Biofuels *8*, 111.

Bowien, B., and Kusian, B. (2002). Genetics and control of CO(2) assimilation in the chemoautotroph Ralstonia eutropha. Arch. Microbiol. *178*, 85–93.

Brilisauer, K., Rapp, J., Rath, P., Schöllhorn, A., Bleul, L., Weiß, E., Stahl, M., Grond, S., and Forchhammer, K. (2019). Cyanobacterial antimetabolite 7-deoxy-sedoheptulose blocks the shikimate pathway to inhibit the growth of prototrophic organisms. Nat. Commun. *10*, 1–11.

Brown, G., Singer, A., Lunin, V.V., Proudfoot, M., Skarina, T., Flick, R., Kochinyan, S., Sanishvili, R., Joachimiak, A., Edwards, A.M., et al. (2009). Structural and biochemical characterization of the type II fructose-1,6-bisphosphatase GlpX from Escherichia coli. J. Biol. Chem. *284*, 3784–3792.

Cai, T., Sun, H., Qiao, J., Zhu, L., Zhang, F., Zhang, J., Tang, Z., Wei, X., Yang, J., Yuan, Q., et al. (2021). Cell-free chemoenzymatic starch synthesis from carbon dioxide. Science *373*, 1523–1527.

Dangel, A.W., and Tabita, F.R. (2015). CbbR, the Master Regulator for Microbial Carbon Dioxide

Fixation. J. Bacteriol. *197*, 3488–3498.

De Porcellinis, A.J., Nørgaard, H., Brey, L.M.F., Erstad, S.M., Jones, P.R., Heazlewood, J.L., and Sakuragi, Y. (2018). Overexpression of bifunctional fructose-1,6-bisphosphatase/sedoheptulose-1,7-bisphosphatase leads to enhanced photosynthesis and global reprogramming of carbon metabolism in Synechococcus sp. PCC 7002. Metab. Eng. *47*, 170–183.

Doello, S., Neumann, N., and Forchhammer, K. (2021). Phosphorylation of phosphoglucomutase 1 on a peripheral site tunes its activity to regulate glycogen metabolism (bioRxiv).

Eisenhut, M., Aguirre von Wobeser, E., Jonas, L., Schubert, H., Ibelings, B.W., Bauwe, H., Matthijs, H.C.P., and Hagemann, M. (2007). Long-term response toward inorganic carbon limitation in wild type and glycolate turnover mutants of the cyanobacterium Synechocystis sp. strain PCC 6803. Plant Physiol. *144*, 1946–1959.

Eisenhut, M., Huege, J., Schwarz, D., Bauwe, H., Kopka, J., and Hagemann, M. (2008). Metabolome phenotyping of inorganic carbon limitation in cells of the wild type and photorespiratory mutants of the cyanobacterium Synechocystis sp. strain PCC 6803. Plant Physiol. *148*, 2109–2120.

Farhat, N., Elkhouni, A., Zorrig, W., Smaoui, A., Abdelly, C., and Rabhi, M. (2016). Effects of magnesium deficiency on photosynthesis and carbohydrate partitioning. Acta Physiol. Plant *38*.

Feng, L., Sun, Y., Deng, H., Li, D., Wan, J., Wang, X., Wang, W., Liao, X., Ren, Y., and Hu, X. (2014a). Structural and biochemical characterization of fructose-1,6/sedoheptulose-1,7-bisphosphatase from the cyanobacterium Synechocystis strain 6803. FEBS J. *281*, 916–926.

Feng, Y., De Franceschi, G., Kahraman, A., Soste, M., Melnik, A., Boersema, P.J., de Laureto, P.P., Nikolaev, Y., Oliveira, A.P., and Picotti, P. (2014b). Global analysis of protein structural changes in complex proteomes. Nat. Biotechnol. *32*, 1036–1044.

Flügel, F., Timm, S., Arrivault, S., Florian, A., Stitt, M., Fernie, A.R., and Bauwe, H. (2017). The Photorespiratory Metabolite 2-Phosphoglycolate Regulates Photosynthesis and Starch Accumulation in Arabidopsis. Plant Cell *29*, 2537–2551.

Foster, C., Boorla, V.S., Dash, S., Gopalakrishnan, S., Jacobson, T.B., Olson, D.G., Amador-Noguez, D., Lynd, L.R., and Maranas, C.D. (2022). Assessing the impact of substrate-level enzyme regulations limiting ethanol titer in Clostridium thermocellum using a core kinetic model. Metab. Eng. *69*, 286–301.

Fu, L., Niu, B., Zhu, Z., Wu, S., and Li, W. (2012). CD-HIT: accelerated for clustering the next-generation sequencing data. Bioinformatics *28*, 3150–3152.

Gopalakrishnan, S., Pakrasi, H.B., and Maranas, C.D. (2018). Elucidation of photoautotrophic carbon flux topology in Synechocystis PCC 6803 using genome-scale carbon mapping models. Metab. Eng. *47*, 190–199.

Grenz S, Baumann PT, Rückert C, Nebel BA, Siebert D, Schwentner A, Eikmanns BJ, Hauer B, Kalinowski J, Takors R, Blombach B (2019). Exploiting Hydrogenophaga pseudoflava for aerobic syngas-based production of chemicals. Metabolic Engineering *55*, 220–230.

Guerreiro, A.C.L., Penning, R., Raaijmakers, L.M., Axman, I.M., Heck, A.J.R., and Altelaar, A.F.M. (2016). Monitoring light/dark association dynamics of multi-protein complexes in cyanobacteria using size exclusion chromatography-based proteomics. J. Proteomics *142*, 33–44.

Hackett, S.R., Zanotelli, V.R.T., Xu, W., Goya, J., Park, J.O., Perlman, D.H., Gibney, P.A., Botstein, D., Storey, J.D., and Rabinowitz, J.D. (2016). Systems-level analysis of mechanisms regulating yeast metabolic flux. Science *354*.

Hauf, W., Schlebusch, M., Hüge, J., Kopka, J., Hagemann, M., and Forchhammer, K. (2013). Metabolic Changes in Synechocystis PCC6803 upon Nitrogen-Starvation: Excess NADPH Sustains Polyhydroxybutyrate Accumulation. Metabolites *3*, 101–118.

Hines, J.K., Fromm, H.J., and Honzatko, R.B. (2006). Novel allosteric activation site in Escherichia coli fructose-1,6-bisphosphatase. J. Biol. Chem. *281*, 18386–18393.

Holland, S.C., Kappell, A.D., and Burnap, R.L. (2015). Redox changes accompanying inorganic carbon limitation in Synechocystis sp. PCC 6803. Biochim. Biophys. Acta *1847*, 355–363.

Jablonsky, J., Papacek, S., and Hagemann, M. (2016). Different strategies of metabolic regulation in cyanobacteria: from transcriptional to biochemical control. Sci. Rep. *6*, 33024.

Jahn, M., Vialas, V., Karlsen, J., Maddalo, G., Edfors, F., Forsström, B., Uhlén, M., Käll, L., and Hudson, E.P. (2018). Growth of Cyanobacteria Is Constrained by the Abundance of Light and Carbon Assimilation Proteins. Cell Rep. *25*, 478–486.e8.

Jahn, M., Crang, N., Janasch, M., Hober, A., Forsström, B., Kimler, K., Mattausch, A., Chen, Q., Asplund-Samuelsson, J., and Hudson, E.P. (2021). Protein allocation and utilization in the versatile chemolithoautotroph Cupriavidus necator. eLife

Jaiswal, D., and Wangikar, P.P. (2020). Dynamic Inventory of Intermediate Metabolites of Cyanobacteria in a Diurnal Cycle. iScience *23*, 101704.

Janasch, M., Asplund-Samuelsson, J., Steuer, R., and Hudson, E.P. (2019). Kinetic modeling of the Calvin cycle identifies flux control and stable metabolomes in Synechocystis carbon fixation. J. Exp. Bot. *70*, 973–983.

Katoh, K., and Standley, D.M. (2013). MAFFT multiple sequence alignment software version 7: improvements in performance and usability. Mol. Biol. Evol. *30*, 772–780.

Klähn, S., Orf, I., Schwarz, D., Matthiessen, J.K.F., Kopka, J., Hess, W.R., and Hagemann, M. (2015). Integrated Transcriptomic and Metabolomic Characterization of the Low-Carbon Response Using an ndhR Mutant of Synechocystis sp. PCC 6803. Plant Physiol. *169*, 1540–1556.

Knoop, H., Gründel, M., Zilliges, Y., Lehmann, R., Hoffmann, S., Lockau, W., and Steuer, R. (2013). Flux balance analysis of cyanobacterial metabolism: the metabolic network of Synechocystis sp. PCC 6803. PLoS Comput. Biol. *9*, e1003081.

Kobayashi, D., Tamoi, M., Iwaki, T., Shigeoka, S., and Wadano, A. (2003). Molecular characterization and redox regulation of phosphoribulokinase from the cyanobacterium Synechococcus sp. PCC 7942. Plant Cell Physiol. *44*, 269–276.

Koch, M., Bruckmoser, J., Scholl, J., Hauf, W., Rieger, B., and Forchhammer, K. (2020). Maximizing PHB content in Synechocystis sp. PCC 6803: a new metabolic engineering strategy based on the regulator PirC. Microb. Cell Fact. *19*, 231.

Kochanowski, K., Volkmer, B., Gerosa, L., Haverkorn van Rijsewijk, B.R., Schmidt, A., and Heinemann, M. (2013). Functioning of a metabolic flux sensor in Escherichia coli. Proc. Natl. Acad. Sci. U. S. A. *110*, 1130–1135.

Kopka, J., Schmidt, S., Dethloff, F., Pade, N., Berendt, S., Schottkowski, M., Martin, N., Dühring, U., Kuchmina, E., Enke, H., et al. (2017). Systems analysis of ethanol production in the genetically engineered cyanobacterium sp. PCC 7002. Biotechnol. Biofuels *10*, 56.

Krieg, T., Sydow, A., Faust, S., Huth, I., and Holtmann, D. (2018). CO2to Terpenes: Autotrophic and Electroautotrophic α-Humulene Production withCupriavidus necator. Angewandte Chemie *130*, 1897–1900.

Kusian, B., and Bowien, B. (1997). Organization and regulation of cbb CO2 assimilation genes in autotrophic bacteria. FEMS Microbiol. Rev. *21*, 135–155.

Lempp, M., Farke, N., Kuntz, M., Freibert, S.A., Lill, R., and Link, H. (2019). Systematic identification of metabolites controlling gene expression in E. coli. Nat. Commun. *10*, 1–9.

Li, W., and Godzik, A. (2006). Cd-hit: a fast program for clustering and comparing large sets of protein

or nucleotide sequences. Bioinformatics *22*, 1658–1659.

Li, G., Hu, Y., Zrimec, J., Luo, H., Wang, H., Zelezniak, A., Ji, B., and Nielsen, J. (2021). Bayesian genome scale modelling identifies thermal determinants of yeast metabolism. Nat. Commun. *12*, 1–12.

Li, J., Yokosho, K., Liu, S., Cao, H.R., Yamaji, N., Zhu, X.G., Liao, H., Ma, J.F., and Chen, Z.C. (2020). Diel magnesium fluctuations in chloroplasts contribute to photosynthesis in rice. Nat Plants *6*, 848–859.

Li, X., Gianoulis, T.A., Yip, K.Y., Gerstein, M., and Snyder, M. (2010). Extensive in vivo metabolite-protein interactions revealed by large-scale systematic analyses. Cell *143*, 639–650.

Liang, F., and Lindblad, P. (2016). Effects of overexpressing photosynthetic carbon flux control enzymes in the cyanobacterium Synechocystis PCC 6803. Metab. Eng. *38*, 56–64.

Lindahl, M., and Kieselbach, T. (2009). Disulphide proteomes and interactions with thioredoxin on the track towards understanding redox regulation in chloroplasts and cyanobacteria. J. Proteomics *72*, 416–438.

Link, H., Kochanowski, K., and Sauer, U. (2013). Systematic identification of allosteric protein-metabolite interactions that control enzyme activity in vivo. Nat. Biotechnol. *31*, 357–361.

Liu, X., Miao, R., Lindberg, P., and Lindblad, P. (2019). Modular engineering for efficient photosynthetic biosynthesis of 1-butanol from CO2in cyanobacteria. Energy & Environmental Science *12*, 2765–2777.

Löwe, H., Beentjes, M., Pflüger-Grau, K., and Kremling, A. (2021). Trehalose production by Cupriavidus necator from CO and hydrogen gas. Bioresour. Technol. *319*, 124169.

Makowka, A., Nichelmann, L., Schulze, D., Spengler, K., Wittmann, C., Forchhammer, K., and Gutekunst, K. (2020). Glycolytic Shunts Replenish the Calvin-Benson-Bassham Cycle as Anaplerotic Reactions in Cyanobacteria. Mol. Plant *13*, 471–482.

Markert, B., Stolzenberger, J., Brautaset, T., and Wendisch, V.F. (2014). Characterization of two transketolases encoded on the chromosome and the plasmid pBM19 of the facultative ribulose monophosphate cycle methylotroph Bacillus methanolicus. BMC Microbiol. *14*, 7.

Martell, A.E., and Smith, R.M. (2013). Critical Stability Constants: First Supplement (Springer US).

Martin, W., Scheibe, R., and Schnarrenberger, C. (2000). The Calvin Cycle and Its Regulation. Photosynthesis 9–51.

Mateus, A., Bobonis, J., Kurzawa, N., Stein, F., Helm, D., Hevler, J., Typas, A., and Savitski, M.M. (2018). Thermal proteome profiling in bacteria: probing protein state. Mol. Syst. Biol. *14*, e8242.

Mateus, A., Savitski, M.M., and Piazza, I. (2021). The rise of proteome-wide biophysics. Mol. Syst. Biol. *17*, e10442.

McKinlay, J.B., and Harwood, C.S. (2010). Carbon dioxide fixation as a central redox cofactor recycling mechanism in bacteria. Proc. Natl. Acad. Sci. U. S. A. *107*, 11669–11675.

Mettler, T., Mühlhaus, T., Hemme, D., Schöttler, M.-A., Rupprecht, J., Idoine, A., Veyel, D., Pal, S.K., Yaneva-Roder, L., Winck, F.V., et al. (2014). Systems Analysis of the Response of Photosynthesis, Metabolism, and Growth to an Increase in Irradiance in the Photosynthetic Model Organism Chlamydomonas reinhardtii. Plant Cell *26*, 2310–2350.

Meyer, O., and Schlegel, H.G. (1978). Reisolation of the carbon monoxide utilizing hydrogen bacterium Pseudomonas carboxydovorans (Kistner) comb. nov. Arch. Microbiol. *118*, 35–43.

Michelet, L., Zaffagnini, M., Morisse, S., Sparla, F., Pérez-Pérez, M.E., Francia, F., Danon, A., Marchand, C.H., Fermani, S., Trost, P., et al. (2013). Redox regulation of the Calvin-Benson cycle: something old, something new. Front. Plant Sci. *4*, 470.

Müller, J., MacEachran, D., Burd, H., Sathitsuksanoh, N., Bi, C., Yeh, Y.-C., Lee, T.S., Hillson, N.J., Chhabra, S.R., Singer, S.W., et al. (2013). Engineering of Ralstonia eutropha H16 for autotrophic and heterotrophic production of methyl ketones. Appl. Environ. Microbiol. *79*, 4433–4439.

Murabito, E., Verma, M., Bekker, M., Bellomo, D., Westerhoff, H.V., Teusink, B., and Steuer, R. (2014). Monte-Carlo Modeling of the Central Carbon Metabolism of Lactococcus lactis: Insights into Metabolic Regulation. PLoS ONE *9*, e106453.

Nishiguchi, H., Liao, J., Shimizu, H., and Matsuda, F. (2020). Novel allosteric inhibition of phosphoribulokinase identified by ensemble kinetic modeling of sp. PCC 6803 metabolism. Metab Eng Commun *11*, e00153.

Nogales, J., Gudmundsson, S., Knight, E.M., Palsson, B.O., and Thiele, I. (2012). Detailing the optimality of photosynthesis in cyanobacteria through systems biology analysis. Proc. Natl. Acad. Sci. U. S. A. *109*, 2678–2683.

Noor, E., Bar-Even, A., Flamholz, A., Reznik, E., Liebermeister, W., and Milo, R. (2014). Pathway thermodynamics highlights kinetic obstacles in central metabolism. PLoS Comput. Biol. *10*, e1003483.

Park, J.M., Kim, T.Y., and Lee, S.Y. (2011). Genome-scale reconstruction and in silico analysis of the Ralstonia eutropha H16 for polyhydroxyalkanoate synthesis, lithoautotrophic growth, and 2-methyl citric acid production. BMC Syst. Biol. *5*, 101.

Pattanayak GK, Liao Y, Wallace EWJ, Budnik B, Drummond DA, Rust MJ (2020). Daily Cycles of Reversible Protein Condensation in Cyanobacteria. Cell Reports *32*, 108032.

Pecoraro, V.L., Hermes, J.D., and Cleland, W.W. (1984). Stability constants of Mg2+ and Cd2+ complexes of adenine nucleotides and thionucleotides and rate constants for formation and dissociation of MgATP and MgADP. Biochemistry *23*, 5262–5271.

Pettersson, G., and Ryde-Pettersson, U. (1989). Dependence of the Calvin cycle activity on kinetic parameters for the interaction of non-equilibrium cycle enzymes with their substrates. Eur. J. Biochem. *186*, 683–687.

Piazza, I., Beaton, N., Bruderer, R., Knobloch, T., Barbisan, C., Chandat, L., Sudau, A., Siepe, I., Rinner, O., de Souza, N., et al. (2020). A machine learning-based chemoproteomic approach to identify drug targets and binding sites in complex proteomes. Nat. Commun. *11*, 1–13.

Piazza I, Kochanowski K, Cappelletti V, Fuhrer T, Noor E, Sauer U, Picotti P (2018). A Map of Protein-Metabolite Interactions Reveals Principles of Chemical Communication. Cell *172*, 358–372.e23.

Pohlmann, A., Fricke, W.F., Reinecke, F., Kusian, B., Liesegang, H., Cramm, R., Eitinger, T., Ewering, C., Pötter, M., Schwartz, E., et al. (2006). Genome sequence of the bioplastic-producing “Knallgas” bacterium Ralstonia eutropha H16. Nature Biotechnology *24*, 1257–1262.

Price, M.N., Dehal, P.S., and Arkin, A.P. (2010). FastTree 2--approximately maximum-likelihood trees for large alignments. PLoS One *5*, e9490.

Raines, C.A. (2003). The Calvin cycle revisited. Photosynth. Res. *75*, 1–10.

Reder, C. (1990). The Structural Approach to Metabolic Control Analysis I: Theoretical Aspects. Control of Metabolic Processes 121–127.

Sarkar, D., Mueller, T.J., Liu, D., Pakrasi, H.B., and Maranas, C.D. (2019). A diurnal flux balance model of Synechocystis sp. PCC 6803 metabolism. PLoS Comput. Biol. *15*, e1006692.

Savitski, M.M., Reinhard, F.B.M., Franken, H., Werner, T., Savitski, M.F., Eberhard, D., Martinez Molina, D., Jafari, R., Dovega, R.B., Klaeger, S., et al. (2014). Tracking cancer drugs in living cells by thermal profiling of the proteome. Science *346*, 1255784.

Schuster, R., and Holzhütter, H.G. (1995). Use of mathematical models for predicting the metabolic

effect of large-scale enzyme activity alterations. Application to enzyme deficiencies of red blood cells. Eur. J. Biochem. *229*, 403–418.

Schwarz, D., Nodop, A., Hüge, J., Purfürst, S., Forchhammer, K., Michel, K.P., Bauwe, H., Kopka, J., and Hagemann, M. (2011). Metabolic and transcriptomic phenotyping of inorganic carbon acclimation in the Cyanobacterium Synechococcus elongatus PCC 7942. Plant Physiol. *155*.

Selim, K.A., Haase, F., Hartmann, M.D., Hagemann, M., and Forchhammer, K. (2018). PII-like signaling protein SbtB links cAMP sensing with cyanobacterial inorganic carbon response. Proceedings of the National Academy of Sciences *115*, E4861–E4869.

Singh, A.K., Santos-Merino, M., Sakkos, J.K., Walker, B.J., and Ducat, D.C. (2022). Rubisco Regulation in Response to Altered Carbon Status in the Cyanobacterium Synechococcus elongatus PCC 7942. Plant Physiol.

Stolzenberger, J., Lindner, S.N., Persicke, M., Brautaset, T., and Wendisch, V.F. (2013). Characterization of fructose 1,6-bisphosphatase and sedoheptulose 1,7-bisphosphatase from the facultative ribulose monophosphate cycle methylotroph Bacillus methanolicus. J. Bacteriol. *195*, 5112–5122.

Tamoi, M., Ishikawa, T., Takeda, T., and Shigeoka, S. (1996). Molecular characterization and resistance to hydrogen peroxide of two fructose-1,6-bisphosphatases from Synechococcus PCC 7942. Arch. Biochem. Biophys. *334*, 27–36.

Tan, C.S.H., Go, K.D., Bisteau, X., Dai, L., Yong, C.H., Prabhu, N., Ozturk, M.B., Lim, Y.T., Sreekumar, L., Lengqvist, J., et al. (2018). Thermal proximity coaggregation for system-wide profiling of protein complex dynamics in cells. Science *359*, 1170–1177.

Tanaka, K., Shimakawa, G., Tabata, H., Kusama, S., Miyake, C., and Nakanishi, S. (2021). Quantification of NAD(P)H in cyanobacterial cells by a phenol extraction method. Photosynth. Res. *148*, 57–66.

Vardakou, M., Salmon, M., Faraldos, J.A., and O'Maille, P.E. (2014). Comparative analysis and validation of the malachite green assay for the high throughput biochemical characterization of terpene synthases. MethodsX *1*, 187–196.

Veyel, D., Sokolowska, E.M., Moreno, J.C., Kierszniowska, S., Cichon, J., Wojciechowska, I., Luzarowski, M., Kosmacz, M., Szlachetko, J., Gorka, M., et al. (2018). PROMIS, global analysis of PROtein-metabolite interactions using size separation in. J. Biol. Chem. *293*, 12440–12453.

Wang, H., Marcišauskas, S., Sánchez, B.J., Domenzain, I., Hermansson, D., Agren, R., Nielsen, J., and Kerkhoven, E.J. (2018). RAVEN 2.0: A versatile toolbox for metabolic network reconstruction and a case study on Streptomyces coelicolor. PLoS Comput. Biol. *14*, e1006541.

Werner, A., Broeckling, C.D., Prasad, A., and Peebles, C.A.M. (2019). A comprehensive time-course metabolite profiling of the model cyanobacterium Synechocystis sp. PCC 6803 under diurnal light:dark cycles. Plant J. *99*, 379–388.

Wilkinson, H.C., and Dalby, P.A. (2020). The Two-Species Model of transketolase explains donor substrate-binding, inhibition and heat-activation. Sci. Rep. *10*, 1–10.

Wolf, N.M., Gutka, H.J., Movahedzadeh, F., and Abad-Zapatero, C. (2018). Structures of the Mycobacterium tuberculosis GlpX protein (class II fructose-1,6-bisphosphatase): implications for the active oligomeric state, catalytic mechanism and citrate inhibition. Acta Crystallogr D Struct Biol *74*, 321–331.

Woolston, B.M., King, J.R., Reiter, M., Van Hove, B., and Stephanopoulos, G. (2018). Improving formaldehyde consumption drives methanol assimilation in engineered E. coli. Nat. Commun. *9*, 2387.

Yu King Hing, N., Liang, F., Lindblad, P., and Morgan, J.A. (2019). Combining isotopically non-stationary metabolic flux analysis with proteomics to unravel the regulation of the Calvin-Benson-Bassham cycle in Synechocystis sp. PCC 6803. Metab. Eng. *56*, 77–84.

Yu King Hing, N., Aryal, U.K., and Morgan, J.A. (2021). Probing light-dependent regulation of the Calvin cycle using a multi-omics approach. Front. Plant Sci. *12*.

Zampieri, M., Hörl, M., Hotz, F., Müller, N.F., and Sauer, U. (2019). Regulatory mechanisms underlying coordination of amino acid and glucose catabolism in Escherichia coli. Nat. Commun. *10*, 1–13.

Zavřel, T., Faizi, M., Loureiro, C., Poschmann, G., Stühler, K., Sinetova, M., Zorina, A., Steuer, R., and Červený, J. (2019). Quantitative insights into the cyanobacterial cell economy. Elife *8*.